Upconverting Luminescence Imaging and Tomography for Biomedical Applications
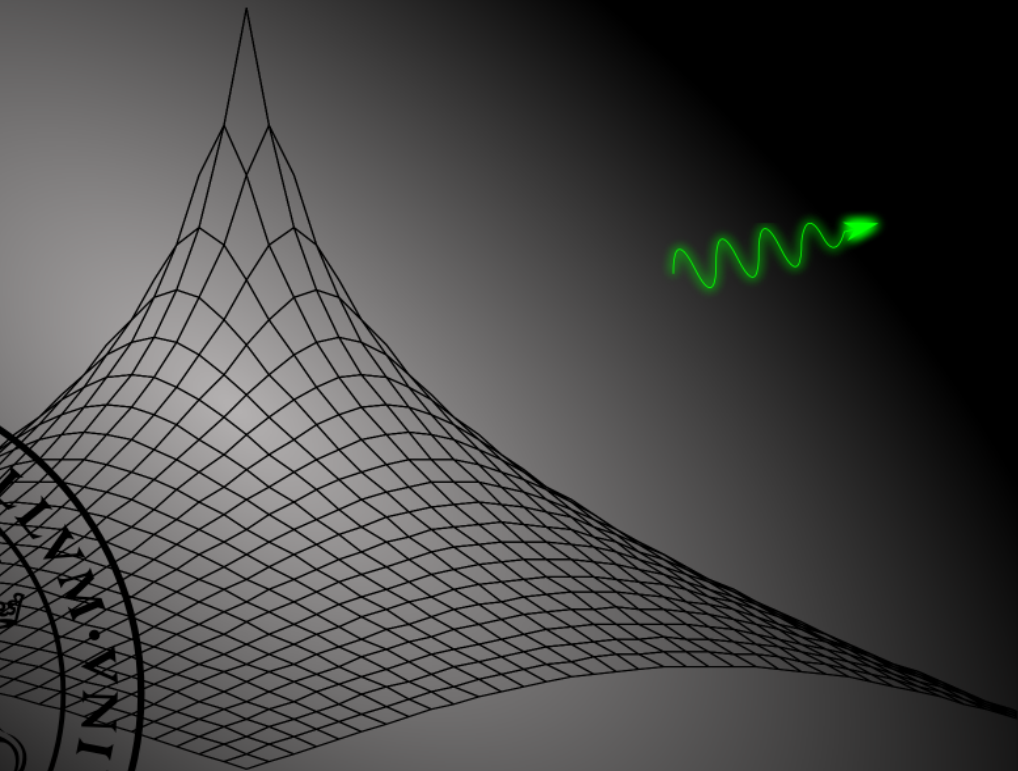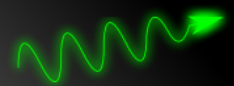
Niclas Svensson Can Xu

Upconverting Luminescence Imaging and Tomography for Biomedical Applications — Populärvetenskaplig sammanfattning

Niclas Svensson och Can Xu

12 november 2008

Optiska markörer är viktiga inom den biomedicinska forskningen. Tack vare stora framsteg inom biotekniken kan idag markörmolekyler bindas på molekyler som söker sig till intressanta områden i organismer. T. ex. används detta för att studera tumörer på ett tidigt stadium samt att studera intressanta ämnen vid Alzheimers sjukdom och andra demenssjukdomar. På detta sätt kan sjukdomsförlopp och påverkan av olika medicinska behandlingar följas. Fokus ligger på funktionell avbildning, att kunna följa förlopp i ett djur eller en människa över tiden.

En viktig typ av markörer är optiska markörer och årets (2008) Nobelpris i kemi har tilldelats Shimomura, Chalfie och Tsien för deras upptäckt och utveckling av grönt fluorescerande protein (GFP), vilket är just en sådan. Fluorescens är när en molekyl absorberar ljus (excitation) för att sedan sända ut ljus (emission), vilket på grund av energikonservering alltid har en längre våglängd. Med hjälp av ett optiskt filter kan excitationsljuset tas bort och det utsända fluorescensljuset detekteras. På så sätt går det med hjälp av en känslig kamera att få en bild över fördelningen av de fluorescerande markörerna, de så kallade fluoroforerna.

Många molekyler som ingår i vävnad är i sig fluorescerande. Fenomenet går under beteckningen autofluorescens. Detta försvårar arbetet med att upptäcka små koncentrationer av fluorescensmarkörer eftersom signalen döljs i den alltid förekommande autofluorescensen.

I detta arbete undersöks möjligheten att använda en ny sorts optiska markörer. Dessa är en sorts nanopartiklar vilka sänder ut ljus med en kortare våglängd än den våglängd de exciteras med. De nanopartiklar som används har erhållits genom ett samarbete med Harbin Institute of Technology i Kina. Nanopartiklarna exciteras med infrarött ljus (980 nm) och emitterar ljus med våglängden 800 nm. Båda dessa våglängder ligger i ett intervall där vävnad är relativt genomskinligt, vävnadens så kallade diagnostiska fönstret, ca 600-1300 nm. Autofluorescens har som nämnt ovan alltid en längre våglängd än excitationsljuset. Eftersom dessa nya markörer har en kortare våglängd, hamnar det utsända ljuset i ett våglängdsområde där det inte förekommer någon autofluorescens. Därför döljs inte signalen från nanopartiklarna i autofluorescensen och med hjälp av optiska filter kan den därför lätt urskiljas.

Nyckelkoncept

- Organiska fluoroforer och kvantprickar avger alltid ljus med en längre våglängd än den de exciteras med. I det här arbetet används en ny sorts nanopartiklar som åstadkommer det motsatta.

- Autofluorescens förekommer alltid i vävnad. och döljer signalen från organiska fluoroforer, men ej från de nya nanopartiklarna.

- Nanopartiklarna både exciteras och avger ljus på våglängder där vävnad är relativt genomskinligt. Att uppnå detta med kvantprickar har visat sig vara svårt.

En mus under fluorescensavbildning. Här används en röd laser för exciation. Lägg märke till hur genomskinlig vävnaden är för rött ljus. En fluorescenskontrast har injecerats i musen och med hjälp av optiska filter kan signalen från denna urskiljas.
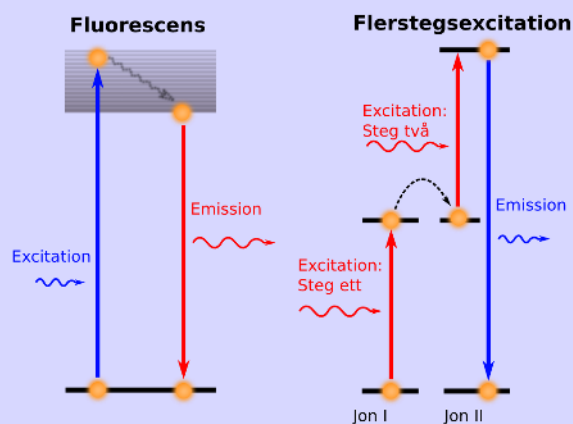
Fysikaliska processer

I den moderna fysiken kan ljus beskrivas som partiklar, så kallade fotoner. Material som träffas av fotoner kan absorbera dessa. Under denna process exciteras materialets elektroner och materialet hamnar i ett högre energitillstånd. Materialet återgår spontant till det lägre energitillståndet, varvid en foton åter bildas och ljus sänds ut. Den senare processen kallas emission.

De flesta material emitterar fotoner av lägre energier än de fotoner som används för excitationen på grund av förluster. Detta illustreras i den vänstra figuren. Här exciteras ett material av blått ljus och emitterar rött ljus.

I detta arbete används en ny sorts material som kan emittera fotoner av kortare våglängd än excitationsvåglängden, vilket kräver excitation av flera fotoner för att energin ska bevaras. Ett exempel av processen illustreras i den högra figuren. Här exciteras en elektron av två röda fotoner för att sedan sända ut en foton av blått ljus.

Fluorescens

Excitation

Emission

Flerstegsexcitation

Excitation: Steg två

Excitation: Steg ett

Emission

Jon I   Jon II

Resultat

Denna figur illustrerar kontrastskillnaden mellan organiska fluorophorer och nanopartiklar i en omgivning innehållande autofluorescens. Resultaten har publicerats i den vetenskapliga tidsskriften Applied Physics Letters, 93, 171103 (2008).

Organisk fluorofor   **Nanopartiklar**

Utan autofluorescens

Med autofluorescens
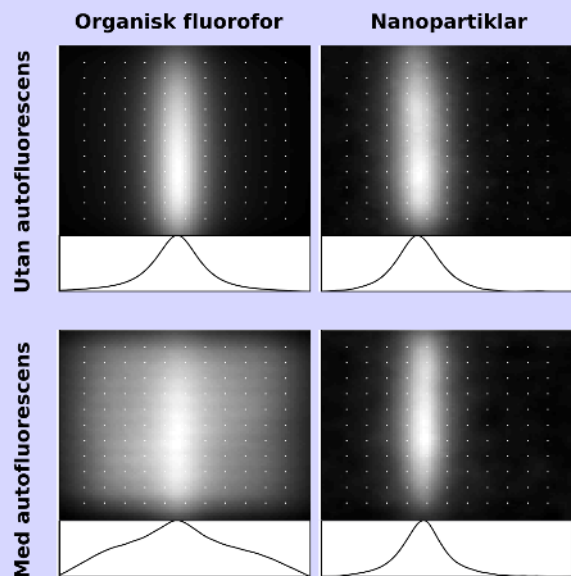
För att efterlikna vävnad, har fantomer med realistiska optiska egenskaper tillverkats. Dessa konstruerades även för att simulera autofluorescens. I dessa placerades ett rör innehållande en lösning av nanopartiklarna, samt ett rör med organiska fluoroforer. Som excitationsljus användes laserdioder, vilka är billiga och lättillgängliga. En bild av det utsända fluorescensljuset erhölls med hjälp av en känslig digitalkamera och lämpliga filter för att ta bort excitationsljuset. I arbetet undersöks också de teoretiska möjligheterna för att använda nanopartiklarna för att göra optisk tomografi. Tomografi går ut på att från ett flertal mätningar återskapa fördelningen av markörerna i tre dimensioner och är ett teoretiskt mycket komplext problem, speciellt för ljus, vilket sprids mycket starkt i vävnad.

I arbetet visas att de nya nanopartiklarna kan användas som optiska markörer på ett sätt som är helt okänsligt för autofluorescens. Teoretiskt visas också att det är möjligt att med hjälp av tomografiska metoder skapa en tredimensionell bild över partiklarnas fördelning. Dock kvarstår mycket arbete innan dessa kan användas i praktiska tillämpningar. Dels måste det förvissas att partiklarna inte är giftiga, dels måste de modifieras så att de kan bindas kemiskt till molekyler med intressanta biologiska egenskaper, t. ex. tumörsökande egenskaper.

Upconverting Luminescence Imaging and Tomography for Biomedical Applications

Niclas Svensson and Can Xu

Master Thesis

2008

LUND UNIVERSITY

UPCONVERTING LUMINESCENCE IMAGING AND TOMOGRAPHY FOR BIOMEDICAL APPLICATIONS

Abstract

Tissue optics is a field devoted to study the interaction of light with tissue. Over the last decades, much thanks to the field of optical spectroscopy, the knowledge of tissue optics has been steadily increasing. This has catalyzed the interest in applying tissue optics as a clinical tool.

This thesis studies an area within tissue optics dealing with fluorescence molecular imaging and tomography. For most visible wavelengths, light does not penetrate more than a few millimeters into tissue. But in the diagnostic window ($\sim$ 600 to 1600 nm), penetration up to several centimeters is possible. This opens up the possibility of imaging fluorescent contrast agents deep in tissue. Fluorescent imaging has a notable importance in biomedical applications. Shimomura, Chalfie and Tsien were recently rewarded with the Nobel prize for discovering and developing the green fluorescent protein, which has become a very important fluorescent marker. Fluorescent imaging can, for example, be used to study biological responses from drugs in small animals over a period of time, without the need to sacrifice them. Currently, considerable amount of research are being performed to enable three-dimensional reconstructions of contrast agent distributions inside animals, so called fluorescent tomography.

The area of fluorescent imaging and tomography has long been adversely affected by the ever-present endogenous tissue autofluorescence. The autofluorescence conceals the signal from the contrast agents when using Stokes-shifted fluorophores, effectively limiting the signal-to-background sensitivity. In this thesis, it is shown that by replacing the traditional Stokes-shifted fluorophores with upconverting nanocrystals, it is possible to avoid the nuisance of autofluorescence. The nanoparticles emit light of a shorter wavelength than their excitation wavelength, effectively shifting the signal to a wavelength region where no autofluorescence is present.

Experiments on tissue phantoms, with realistic optical properties, were performed, and it was shown that it is possible to detect an autofluorescence-free signal. Also a theoretical framework for using the nanocrystals for three-dimensional tomographic reconstruction was derived. Simulations were performed based on this framework, showing promising results. Based on the results presented in this thesis, we believe that upconverting nanocrystals may very well be envisaged as important biological markers for tissue imaging purposes.

Table of Physical Quantities

Symbol	Physical quantity	Definition	Units
$\phi(\mathbf{r}, \hat{\mathbf{s}})$	Radiance		$\mathrm{W/m^2 sr}$
$\Phi(\mathbf{r})$	Fluence rate	$\Phi(\mathbf{r}) = \int_{4\pi} \phi(\mathbf{r}, \hat{\mathbf{s}})\, \mathrm{d}\Omega$	$\mathrm{W/m^2}$
n	Refractive index		-
c	Speed of light in tissue	$c = c_0/n$	m/s
μ_a	Absorption coefficient		1/m
μ_s	Scattering coefficient		1/m
μ_tr	Transport attenuation coefficient	$\mu_\mathrm{tr} = \mu_\mathrm{a} + \mu_\mathrm{s}$	1/m
g	Scattering asymmetry parameter		–
μ_s'	Reduced scattering coefficient	$\mu_\mathrm{s}' = (1-g)\mu_\mathrm{s}$	1/m
κ	Diffusion coefficient	$\kappa = 1/3(\mu_\mathrm{s}' + \mu_\mathrm{a})$	m
μ_eff	Effective attenuation coefficient	$\mu_\mathrm{eff} = \sqrt{\mu_\mathrm{a}/\kappa}$	1/m
η	Upconversion efficiency	$\eta = I(\omega_\mathrm{f})/I(\omega_\mathrm{e})$	-
η_2p	Upconversion two-photon efficiency	$\eta_\mathrm{2p} = I(\omega_\mathrm{f})/I(\omega_\mathrm{e})^2$	$\mathrm{m^2/W}$

Definitions

The Fourier transform of a function $f(\mathbf{r}, t)$, of the variables $\mathbf{r} = (x, y, z)$ and t is [1]

$$\widetilde{f}(\mathbf{k}, \omega) = \iint f(\mathbf{r}, t) \mathrm{e}^{\mathrm{i}(\mathbf{k}\cdot\mathbf{r} - \omega t)}\, \mathrm{d}\mathbf{r}^3\, \mathrm{d}t, \tag{1}$$

and the inverse transform is

$$f(\mathbf{r}, t) = \frac{1}{(2\pi)^4} \iint \widetilde{f}(\mathbf{k}, \omega) \mathrm{e}^{-\mathrm{i}(\mathbf{k}\cdot\mathbf{r} - \omega t)}\, \mathrm{d}\mathbf{k}^3\, \mathrm{d}\omega. \tag{2}$$

Acknowledgements

First of all, we would like to thank our principal supervisor, Prof. Stefan Andersson-Engels, for letting us become a part of the Medical Laser Group and participate in various activities. You have provided an extremely interesting topic for us to investigate and have always been supportive and innovative during times when we have encountered problems.

The help given by our co-supervisors Johan Axelsson and Pontus Svenmarker is also very much appreciated. We have had plenty of fruitful discussion ranging from technical issues to theoretical issues dealing with diffuse optical tomography. We thank Erik Alerstam and Tomas Svensson for their assistance with the time-of-flight measurements, and Dmitry Khoptyar both for the help with the equipment and for the interesting discussions. We also acknowledge the help given by Zuguang Guan in the LIDAR bus, and Märta Lewander for always being helpful with the light sources.

Prof. Zhang and his group of Harbin Institute of Technology, are gratefully acknowledged for fabricating the particles and choosing to collaborate with us.

Special thanks to Gabriel Somesfalean for his important collaboration work, which provided us with the nanoparticles used in this thesis. Without this important collaboration over the continents, this thesis would not exist!

Finally, we are infinitely grateful for the support provided by our friends and families whom have given us encouragements and motivations when we have needed them the most.

Contents

List of Figures

List of Tables

Introduction

Within the field of tissue optics, light interaction with tissue is studied. Over the last decades, the field has grown rapidly. With increasing knowledge of the light-tissue interaction, the interest in applying tissue optics as a diagnostic tool is also emerging, reaping the fruits from the fundamental research. This thesis explores an area in tissue optics dealing with *fluorescence molecular tomography and imaging*[1] using upconverting crystals as fluorophores. The motivation for choosing such fluorophores is to gain contrast by enable the possibility to build an autofluorescence insensitive system.

This chapter gives an overview of the fundamentals of tissue optics, and a discussion of the theory. In the following chapter, the basic theory of the upconverting nanocrystals will be discussed. In chapter 3, the theory for fluorescent optical tomography using organic fluorophores is introduced along with the modifications to make it applicable on the quadratic nanocrystals used in this work. The results from the experiments and simulations are presented in chapter 4. This present thesis is concluded with a summary of the most important results as well as a discussion of the future possibilities.

1.1 Tissue Optics

Optically, biological tissues are inhomogeneous and absorptive media, with a slightly higher refractive index than water. When light interacts with tissue, multiple scattering and absorption events are expected to occur, where the possibilities for these events are highly wavelength dependent. Since tissue has a high concentration of water, it is an advantage to use light from a wavelength region where the absorption from water is low, this will enforce an ultimate limit on the usable wavelengths. However, in transdermal non-invasive applications, light needs to penetrate the skin which will put further constraints on the usable wavelengths as discussed below.

---

[1]FMT and FMI are known by many names. Some variants are diffuse fluorescence optical tomography/imaging, optical fluorescence tomography/imaging and diffuse fluorescence tomography.
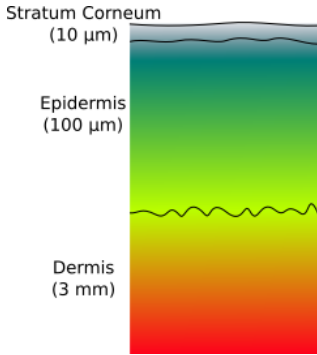
Fig. 1.1: A simple layered model of the human skin. Light at shorter wavelengths has less penetration than light at longer wavelengths.

For simplification, the skin can be seen as a layered structure, with the stratum corneum on top, followed by the epidermis and the dermis below [2, 3], see Fig. 1.1. The stratum corneum and epidermis are very effective in attenuating light, mainly due to high absorption for wavelengths < 300 nm from aromatic amino acids, nucleic acids and urocanic acid. For longer wavelengths, $350 - 1200$ nm, melanin in the epidermis is the major absorber. As light enters the dermis, scattering begins to dominate over absorption. The dermis can thus be described as a turbid tissue matrix [2]. For tissue types below the dermis, scattering usually dominates over absorption [4, 5]. In a crude approximation, the scattering can be modeled using Rayleigh scattering. This implies that light at shorter wavelengths will be much more scattered than light at longer wavelengths.

Considering both the scattering and the absorption in tissue, the transdermal diagnostic window resides in the longer wavelength regions and can be considered to range from 600 nm to 1600 nm [6].[2]

Model of Tissue

In the general model, tissue is considered to consist of an inhomogeneous solution of absorptive particles in water. The nature of the inhomogeneities causes light to scatter heavily. It should be noted that the origin of the scattering effects is not yet fully understood [7].

In a first approximation one can assume that most of the cells and other particles within tissue have spherical or oblate spheroid shapes [6]. As known, Mie theory describes the interaction of light in spherical particles [8], and can in principle be used to calculate the interaction of light with tissue down to a cellular level. Practically, this approach is tricky to realize, both due to the difficulties in obtaining accurate detailed geometries and the time consuming calculations required for detailed geometries.

Instead, tissue is considered to consist of a random continuum of homogeneous sections [6]. Each section can then be described by its absorption coefficient μ_a [m^{-1}], scattering coefficient μ_s [m^{-1}] and anisotropy factor g which describes the expectation value of the direction for a scattered photon. The latter two parameters are usually bundled together into a reduced scattering coefficient $\mu_s' = (1 - g)\mu_s$ within the diffusion approximation.
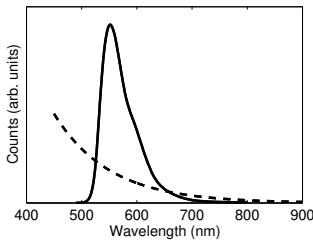
Fig. 1.2: A typical signal with an autofluorescence background. The tissue autofluorescence is in general less Stokes shifted than the commonly used fluorophores. The solid curve represents the signal of interest from an exogenous fluorophore. The dashed curve represents the tissue autofluorescence from endogenous fluorophores.

Tissue Autofluorescence

Tissue contains several endogenous fluorophores which have a strong fluorescence with small Stokes shift when excited by $\lambda < 600$ nm [9, 10, 11]. For longer wavelengths in the diagnostics window, the endogenous autofluorescence from tissue is in general much weaker. However, in many imaging and tomography applications, the signal itself is also weak, thus still limited by the background autofluorescence which causes artifacts. A typical signal with an autofluorescence background spectrum is shown in Fig. 1.2.

---

[2]The range of the diagnostics window is of course not fixed in stone. For example, shorter wavelengths in the blue or ultraviolet regions can be preferred to excite some fluorophores. Nonetheless, light at longer wavelengths will in general result in deeper penetration, and is of the advantage when probing subdermal tissue.

Since the signal and the background autofluorescence often overlaps, separating them is not trivial. Different spectral unmixing algorithms that utilize the spectral characteristics can be used, yielding varying qualities [12]. A more promising approach is to use a fluorophore that emits a signal that is more Stokes shifted than the tissue autofluorescence. Currently, quantum dots are very popular for this approach [13, 14]. Quantum dots are very bright fluorophores that absorb mainly in the ultraviolet (UV) region [15]. This in itself is a drawback, since it is known that using light at short wavelengths is not ideal for transdermal measurements, due to shallow penetration depths and the risks for DNA damage. Furthermore, quantum dots are often fabricated with materials that are highly toxic for organisms. If properly contained and stabilized, this in itself is not an issue. However, studies have shown that quantum dots tend to react when exposed to biological environments and can be very harmful [16, 17].

Upconverting nanocrystals have been proposed as fluorophores in biomedical imaging applications due to their unique property to efficiently emit anti-Stokes shifted light upon near-infrared (NIR) exciation [18, 19]. By intuition, this should mean that the signal can be detected in a region where no autofluorescence is present.

1.2 Light Propagation in Tissue

Light propagation can be described using the electromagnetic wave theory through Maxwell's equations, or the transport theory through the radiative transfer equation (RTE) which is equivalent to Boltzmann's equation in kinetics. Solving Maxwell's equations in tissue has proven to be problematic due to the complexity of biological materials, whereas solving the RTE can provide good solutions that accurately describe the photon transport through the tissue [20].

This section describes the propagation of light in tissue starting with the radiative transfer equation, followed by an overview of important methods for approximating and solving the radiative transfer equation.

The Radiative Transfer Equation

Within tissue, the photon propagation can be described using the radiative transfer equation. Since the particle nature of photons is exploited in favor of their wave nature in RTE, it effectively means that only intensities are considered, and information of for example phase, coherence, polarization and non-linearity is neglected. This is motivated, since the wavelength of the light typically is much smaller than the distance a photon travels between interactions with matter [21].

In its essence, the RTE is derived from the laws of energy conservation. The main parameter of consideration is the radiance $\phi(\mathbf{r}, \hat{\mathbf{s}}, t)$ [W/m^2 sr], which describes the radiant power per unit solid angle along a unit vector $\hat{\mathbf{s}}$ passing through a unit area perpendicular to $\hat{\mathbf{s}}$ at a given time t and position $\mathbf{r}$. Knowing the radiance, it is easy to realize that it must be related to the photon distribution function $N(\mathbf{r}, \hat{\mathbf{s}}, t)$ [m^{-3}sr^{-1}] by

$$\phi(\mathbf{r}, \hat{\mathbf{s}}, t) = N(\mathbf{r}, \hat{\mathbf{s}}, t)h\nu c, \qquad (1.1)$$

where $h\nu$ is the photon energy and c the speed of light in tissue.

Consider a small volume V. Within the volume, the photon distribution will change with time

$$\int \frac{\partial}{\partial t} N(\mathbf{r}, \hat{\mathbf{s}}, t)\, \mathrm{d}V \tag{1.2}$$

for the following reasons:

1) Photons will propagate through the boundaries of the volume:[3]

$$-\int cN(\mathbf{r}, \hat{\mathbf{s}}, t)\hat{\mathbf{s}} \cdot \hat{\mathbf{n}}\, \mathrm{d}A = -\int c\hat{\mathbf{s}} \cdot \nabla N(\mathbf{r}, \hat{\mathbf{s}}, t)\, \mathrm{d}V. \tag{1.3}$$

2) Photons will be lost due to extinction (absorption and scattering):

$$-\int c\mu_{\mathrm{a}}(\mathbf{r})N(\mathbf{r}, \hat{\mathbf{s}}, t)\, \mathrm{d}V - \int c\mu_{\mathrm{s}}(\mathbf{r})N(\mathbf{r}, \hat{\mathbf{s}}, t)\, \mathrm{d}V = -\int c\mu_{\mathrm{tr}}(\mathbf{r})N(\mathbf{r}, \hat{\mathbf{s}}, t)\, \mathrm{d}V. \tag{1.4}$$

3) Photons traveling along other directions can be scattered to travel along $\hat{\mathbf{s}}$:

$$\iint c\mu_{\mathrm{s}}(\mathbf{r})\Theta(\hat{\mathbf{s}} \cdot \hat{\mathbf{s}}')N(\mathbf{r}, \hat{\mathbf{s}}', t)\, \mathrm{d}\Omega'\, \mathrm{d}V. \tag{1.5}$$

$\Theta(\hat{\mathbf{s}} \cdot \hat{\mathbf{s}}')$ is the phase function describing the probability of light traveling along $\hat{\mathbf{s}}'$ to be scattered to travel along $\hat{\mathbf{s}}$ within $\mathrm{d}\Omega'$. The phase function is assumed to be symmetric along the propagation axis and will be further discussed below.

4) Photons can be created within the volume if a source q $[\mathrm{m}^{-3}\ \mathrm{sr}^{-1}\ \mathrm{s}^{-1}]$ is available:

$$\int q(\mathbf{r}, \hat{\mathbf{s}}, t)\, \mathrm{d}V. \tag{1.6}$$

Consolidating (1.2), (1.3), (1.4), (1.5), (1.6), dropping the volume integrals and using (1.1) gives us the RTE,

$$\left(\frac{1}{c}\frac{\partial}{\partial t} + \hat{\mathbf{s}} \cdot \nabla + \mu_{\mathrm{tr}}(\mathbf{r}) \right) \phi(\mathbf{r}, \hat{\mathbf{s}}, t) = \mu_{\mathrm{s}}(\mathbf{r}) \int \Theta(\hat{\mathbf{s}} \cdot \hat{\mathbf{s}}')\phi(\mathbf{r}, \hat{\mathbf{s}}', t)\, \mathrm{d}\Omega' + Q(\mathbf{r}, \hat{\mathbf{s}}, t), \tag{1.7}$$

where

$$Q(\mathbf{r}, \hat{\mathbf{s}}, t) = q(\mathbf{r}, \hat{\mathbf{s}}, t)h\nu. \tag{1.8}$$

We also define the two quantities, fluence rate $\Phi(\mathbf{r}, t)$ and fluence current $\mathbf{J}(\mathbf{r}, t)$, as

$$\Phi(\mathbf{r}, t) = \int \phi(\mathbf{r}, \hat{\mathbf{s}}, t)\, \mathrm{d}\Omega, \tag{1.9}$$

$$\mathbf{J}(\mathbf{r}, t) = \int \hat{\mathbf{s}}\phi(\mathbf{r}, \hat{\mathbf{s}}, t)\, \mathrm{d}\Omega. \tag{1.10}$$

The Henyey-Greenstein Phase Function

The scattering phase function as seen in (1.5) describes the probability of scattering from $\hat{\mathbf{s}}'$ to $\hat{\mathbf{s}}$. Under the assumption that tissue is isotropic in an optical sense, the scattering phase function has the following form,

$$\Theta(\hat{\mathbf{s}} \cdot \hat{\mathbf{s}}') = \Theta(\cos\theta), \tag{1.11}$$

---

[3]Using Gauss' theorem and the relation, $\nabla \cdot (\phi\mathbf{F}) = \phi\nabla \cdot \mathbf{F} + (\nabla\phi) \cdot \mathbf{F}$.

which means that the scattering probability only depend on the angle between $\hat{\mathbf{s}}'$ and $\hat{\mathbf{s}}$. The scattering phase function should also be normalized, meaning that it satisfies

$$\int_{4\pi} \Theta(\hat{\mathbf{s}} \cdot \hat{\mathbf{s}}') \, \mathrm{d}\Omega' = 1. \tag{1.12}$$

Tissues are in general forward scattering media. The forward scattering property agrees with Mie scattering[4], which also predict forward scattering nature for big particles [22, 4]. A commonly used phase function is the Henyey-Greenstein phase function which was originally derived to be used to describe diffuse radiation in galaxies [23]

$$\Theta_{\mathrm{HG}}(\cos\theta) = \frac{1}{4\pi} \frac{1 - g^2}{(1 + g^2 - 2g\cos\theta)^{3/2}}. \tag{1.13}$$

Here, g is a tunable parameter and is usually called the anisotropy factor which is defined as

$$g = \frac{\int_{4\pi} \Theta(\hat{\mathbf{s}} \cdot \hat{\mathbf{s}}')(\hat{\mathbf{s}} \cdot \hat{\mathbf{s}}') \, \mathrm{d}\Omega'}{\int_{4\pi} \Theta(\hat{\mathbf{s}} \cdot \hat{\mathbf{s}}') \, \mathrm{d}\Omega'} = \int_{4\pi} \Theta(\hat{\mathbf{s}} \cdot \hat{\mathbf{s}}')(\hat{\mathbf{s}} \cdot \hat{\mathbf{s}}') \, \mathrm{d}\Omega' = \langle \cos\theta \rangle. \tag{1.14}$$

Figure 1.3 shows (1.13) for three different g-factors. It is worth to notice that the common choice to use the Henyey-Greenstein phase function is by no means trivial, and there are discussions concerning better alternatives [24, 25].
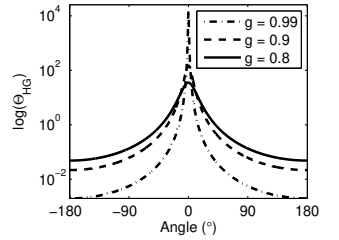

Fig. 1.3: The probability density function for isotropic scattering.

Solution Methods for the Radiative Transport Equation

Analytical solutions to the RTE are scarce at best and only exist for very simple cases such as one dimensional structures [26]. This section describes two methods to find approximative solutions to the RTE.

Monte Carlo Simulation

The first method is Monte Carlo simulation, which has been used for complex physical problems in many different fields dealing with transport equations [27, 28, 29, 30, 31]. In tissue optics, a Monte Carlo simulation sends photons into a predefined medium with known optical properties, and a robust random number generator following the probability distributions in tissue is used to determine the fate of each photon, namely if they are to be scattered, absorbed or refracted for every distance they propagate. A package written in C for running Monte Carlo simulation in multi-layered structures (MCML) has been made available by Wang *et al* [32].

Monte Carlo simulation is actually only a discrete version of the RTE [24] and it can give very accurate results.[5] The tradeoff is the rather time consuming runtime. Due to the linearity of Monte Carlo simulations, it is very well suited for multithreading. A new accelerated method utilizing the parallelism of GPUs[6] has recently been reported [33].

---

[4]The term Mie scattering denotes scattering from spherical particles with sizes comparable of the interesting wavelengths.

[5]This is of course ultimately limited by the accuracy of the input, i.e. the geometry, g-factor, μ_a and μ_s.

[6]Graphics Processing Unit.

P_N Approximations

The second method is to use P_N approximations. These are obtained by expanding the interesting quantities in (1.7) using spherical harmonic expansion. $\phi(\mathbf{r}, \hat{\mathbf{s}}, t)$ and $Q(\mathbf{r}, \hat{\mathbf{s}}, t)$ are thus written as

$$\phi(\mathbf{r}, \hat{\mathbf{s}}, t) = \sum_{l}^{\infty} \sum_{m=-l}^{l} \left(\frac{2l+1}{4\pi} \right)^{\frac{1}{2}} \Psi_{l,m}(\mathbf{r}, t) Y_{l,m}(\hat{\mathbf{s}}), \qquad (1.15)$$

$$Q(\mathbf{r}, \hat{\mathbf{s}}, t) = \sum_{l}^{\infty} \sum_{m=-l}^{l} \left(\frac{2l+1}{4\pi} \right)^{\frac{1}{2}} Q_{l,m}(\mathbf{r}, t) Y_{l,m}(\hat{\mathbf{s}}) . \qquad (1.16)$$

Using the addition theorem [34] the phase function can be expressed as

$$\Theta(\hat{\mathbf{s}} \cdot \hat{\mathbf{s}}') = \sum_{l}^{\infty} \left(\frac{2l+1}{4\pi} \right) \Theta_l P_l(\cos\theta) = \sum_{l}^{\infty} \sum_{m=-l}^{l} \Theta_l Y_{l,m}^*(\hat{\mathbf{s}}') Y_{l,m}(\hat{\mathbf{s}}) . \qquad (1.17)$$

Writing the unit vector $\hat{\mathbf{s}}$ in spherical coordinates

$$\hat{\mathbf{s}} = \begin{pmatrix} s_x \\ s_y \\ s_z \end{pmatrix} = \begin{pmatrix} \sin\theta\cos\varphi \\ \sin\theta\sin\varphi \\ \cos\theta \end{pmatrix}, \qquad (1.18)$$

and inserting (1.15) into (1.9) and (1.10) gives us

$$\Phi(\mathbf{r}, t) \;\; = \;\; \Psi_{0,0}(\mathbf{r}, t) \qquad (1.19)$$

$$\mathbf{J}(\mathbf{r}, t) \;\; = \;\; \begin{pmatrix} \frac{1}{\sqrt{2}}(\Psi_{1,-1}(\mathbf{r}, t) - \Psi_{1,1}(\mathbf{r}, t)) \\ \frac{1}{\mathrm{i}\sqrt{2}}(\Psi_{1,-1}(\mathbf{r}, t) + \Psi_{1,1}(\mathbf{r}, t)) \\ \Psi_{1,0}(\mathbf{r}, t) \end{pmatrix} , \qquad (1.20)$$

where the symmetry and orthogonality properties of the spherical harmonics have been used.

Rewriting (1.7) with the expressions in (1.15) and (1.16), and taking the inner product with $Y_{l,m}^*(\hat{\mathbf{s}})$, the terms in (1.7) decouples and it is possible to rewrite it as [35]

$$\left(\frac{1}{c} \frac{\partial}{\partial t} + \mu_{\mathrm{tr}}(\mathbf{r}) \right) \Psi_{l,m}(\mathbf{r}, t) + \frac{1}{2l+1} \left(\frac{\partial}{\partial z} [(l+1-m)^{\frac{1}{2}}(l+1+m)^{\frac{1}{2}} \Psi_{l+1,m}(\mathbf{r}, t) \right.$$

$$+ (l-m)^{\frac{1}{2}}(l+m)^{\frac{1}{2}} \Psi_{l-1,m}(\mathbf{r}, t)]$$

$$- \frac{1}{2} \left(\frac{\partial}{\partial x} - \mathrm{i} \frac{\partial}{\partial y} \right) [(l+m)^{\frac{1}{2}}(l+m-1)^{\frac{1}{2}} \Psi_{l-1,m-1}(\mathbf{r}, t)]$$

$$- (l-m+2)^{\frac{1}{2}}(l-m+1)^{\frac{1}{2}} \Psi_{l+1,m-1}(\mathbf{r}, t)]$$

$$- \frac{1}{2} \left(\frac{\partial}{\partial x} + \mathrm{i} \frac{\partial}{\partial y} \right) [-(l-m)^{\frac{1}{2}}(l-m-1)^{\frac{1}{2}} \Psi_{l-1,m+1}(\mathbf{r}, t)$$

$$+ (l+m+1)^{\frac{1}{2}}(l+m+2)^{\frac{1}{2}} \Psi_{l+1,m+1}(\mathbf{r}, t)] \Big)$$

$$= \mu_{\mathrm{s}}(\mathbf{r}) \Theta_l \Psi_{l,m}(\mathbf{r}, t) + Q_{l,m}(\mathbf{r}, t) \qquad (1.21)$$

which form an infinite set of coupled equations. The P_N approximations are obtained by assuming $\Psi_{l,m} = 0$ for $l > N$.

P_1 and Diffusion Approximation

The P_1 approximation is obtained by setting $N = 1$. Rewriting (1.21) using (1.9) and (1.10) yields [35]

$$\left(\frac{1}{c}\frac{\partial}{\partial t} + \mu_{\mathrm{tr}}\right)\Phi(\mathbf{r}, t) + \nabla \cdot \mathbf{J}(\mathbf{r}, t) = \mu_{\mathrm{s}}(\mathbf{r})\Phi(\mathbf{r}, t) + \Theta_0 Q_{0,0}(\mathbf{r}, t), \qquad (1.22)$$

$$\left(\frac{1}{c}\frac{\partial}{\partial t} + \mu_{\mathrm{tr}}\right)\mathbf{J}(\mathbf{r}, t) + \frac{1}{3}\nabla\Phi(\mathbf{r}, t) = \Theta_1 \mu_{\mathrm{s}}(\mathbf{r})\mathbf{J}(\mathbf{r}, t) + \mathbf{Q}_1, \qquad (1.23)$$

where

$$\mathbf{Q}_1(\mathbf{r}, t) = \begin{pmatrix} \frac{1}{\sqrt{2}}(Q_{1,-1}(\mathbf{r}, t) - Q_{1,1}(\mathbf{r}, t)) \\ \frac{1}{\mathrm{i}\sqrt{2}}(Q_{1,-1}(\mathbf{r}, t) + Q_{1,1}(\mathbf{r}, t)) \\ Q_{1,0}(\mathbf{r}, t) \end{pmatrix}. \qquad (1.24)$$

Noticing that $\Theta_0 = 1$ and introducing[7]

$$Q_0 = Q_{0,0}, \qquad (1.25)$$

$$\kappa(\mathbf{r}) = \frac{1}{3(\mu_{\mathrm{a}}(\mathbf{r}) + \mu_{\mathrm{s}}'(\mathbf{r}))}, \qquad (1.26)$$

(1.22) and (1.23) can be rearranged to

$$\left(\frac{1}{c}\frac{\partial}{\partial t} + \mu_{\mathrm{a}}(\mathbf{r})\right)\Phi(\mathbf{r}, t) + \nabla \cdot \mathbf{J}(\mathbf{r}, t) = Q_0(\mathbf{r}, t) \qquad (1.27)$$

$$\left(\frac{1}{c}\frac{\partial}{\partial t} + \frac{1}{3\kappa(\mathbf{r})}\right)\mathbf{J}(\mathbf{r}, t) + \frac{1}{3}\nabla\Phi(\mathbf{r}, t) = \mathbf{Q}_1(\mathbf{r}, t). \qquad (1.28)$$

To arrive at the diffusion approximation, two conditions need to be fulfilled:

$$\frac{\partial \mathbf{J}}{\partial t} = 0, \qquad (1.29)$$

$$\mathbf{Q}_1 = 0. \qquad (1.30)$$

Condition (1.29) is automatically fulfilled for steady state problems. For time dependent problems, it has been shown that the condition in the frequency domain holds if $\omega \ll \mu_{\mathrm{s}}'c$ [37]. Condition (1.30) is fulfilled for isotropic sources. This is acceptable in scattering media, where a pencil beam can be treated as an isotropic source placed at a depth of $1/\mu_{\mathrm{s}}'$ from the surface.

Using (1.29) and (1.30) we arrive at the diffusion equation

$$\left(\frac{1}{c}\frac{\partial}{\partial t} + \mu_{\mathrm{a}} - \nabla \cdot \kappa(\mathbf{r})\nabla\right)\Phi(\mathbf{r}, t) = Q_0(\mathbf{r}, t). \qquad (1.31)$$

For most applications, the absorption coefficient is much smaller than the reduced scattering coefficient, which makes the P_1 approximation adequate. However, it is also possible to use P_N approximations of higher orders. Such

---

[7]Whether or not the diffusion constant κ should depend on μ_{a} is a well discussed topic. Furutsu *et al* [36] have shown that it is possible to separate scattering and absorption in the RTE before the P_1 approximation, which physically means that scattering and absorption are independent of each other.

approximations have been shown to provide more accurate results in highly absorptive systems [38]. It also follows that P_N approximations of higher orders will mainly affect the transient, with negligible difference to the diffusion approximation after a delayed time $t_{\mathrm{d}} = r/c$, where r is the radial part using spherical coordinates [35].

It should also be mentioned that the validity of the diffusion approximation is dependent on source-detector separations for some given optical properties. For small source-detector separations, the diffusion approximation is in general not the method of choice [38, 39].

Upconverting Nanocrystals

Upconversion is a process that occurs when two or more photons are absorbed and a photon of higher energy, than those of the incoming photons, is released. The process is most easily observed in materials containing a meta-stable state that can trap one electron for a long time, increasing the interaction-probability with another arriving photon [40]. This concept is employed in infrared markers, where visible light is used to charge the markers to a very long-lived meta-stable state, the markers will then emit visible light when exposed to infrared light.

Under coherent pumping, more complex upconversion phenomenas can be observed. It has been understood that the upconverted luminescence observed under these conditions results from a combination of several processes.

In this work, solids doped with different rare earth ions are used to obtain upconversion.

2.1 Upconversion Processes in Rare Earth-doped Solids

The concept of upconversion in ion-doped solids was first proposed by Bloembergen in 1959 [41]. He described a method to detect infrared radiation by converting it into visible light. However, the intensity of black body radiators were too low to allow the upconversion to work in the way described in the article. Even though upconversion is possible for low intensity light sources, it usually happens due to another process, which will be described in this chapter, rather than the excited state absorption (ESA) process described by Bloembergen. With the invention of the laser, the upconverting processes could be more thoroughly studied. Today, the processes are better understood [42].

The topic has been reviewed by Auzel in 2004 [42], which we refer to when nothing else is specified.

Rare Earth Ions

Solid state upconverting materials are often fabricated by doping the materials with *rare earth ions*. The rare earths fills their outer electron shells before their

inner shells, giving them sharp atomic-like spectral lines, even when bound in solid materials [43, 44]. Upconversion processes involving rare-earth ions have been observed in many types of solid hosts, including crystals, silica fibers and waveguides, as well as bulk materials.

The processes involve energy transfer between rare earth ions of the same kind as well as different kinds. The first ion being excited is called a *sensitizer*, and the ion to which the energy is transferred to is called an *activator*.[1]
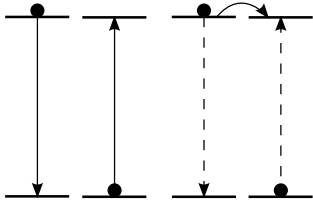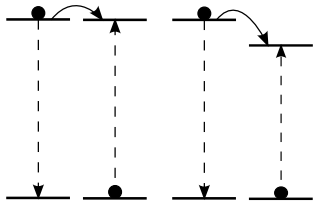
Involved Upconversion Processes

Upconversion can happen due to numerous processes, which impact the upconversion process differently depending on the ion pairs and the excitation intensities.

Some of the processes involve energy transfer between ions. This energy diffusion, can be radiative or non-radiative, resonant or non-resonant, see Fig. 2.1 and Fig. 2.2. In the radiative case, a photon is released from the sensitizer and absorbed by the activator, while in the non-radiative case, the excitation energy will jump from one ion to the other via an electrostatic interaction. The two cases can be experimentally distinguished. The radiative transfer is dependent on the shape of the sample and also affects the emission spectrum as well as the lifetime of the activator. When the transition is non-resonant, it has to be phonon-assisted. The non-resonant transitions are encountered for higher energy differences between rare-earth ions compared to other solid materials, especially in the non-radiative case.

The ETU and ESA processes which are discussed below are illustrated in Fig. 2.3.

ESA (Excited-State Absorption)   Excited state absorptions happen when an ion, being in an excited state, absorbs one more photon. The probability for this process is usually small, and can only be observed under coherent pumping.
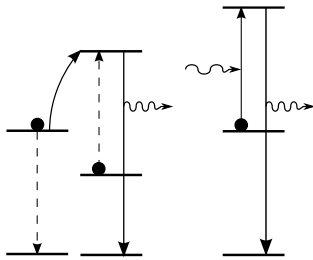
ETU (Energy Transfer Upconversion)   Energy transfer upconversion[2] is a process involving energy transfer between ions. Here, an activator in an excited state is considered. Energy can then be transferred non-radiatively from a sensitizer. This is possible because only energy differences are significant in preserving the energy. This effect is usually efficient and dominating in the most efficient materials.

Cooperative Upconversion   Cooperative upconversion can be of two different kinds, *cooperative sensitization* or *cooperative luminescence*. In the first case, two sensitizers simultaneously give their energies to one activator, and in the second case, two excited ions give away their energies simultaneously, sending out a photon of the double energy.

The Photon Avalanche Effect   The photon avalanche effect is very complex and has been given its name because the resemblance to the avalanche

Fig. 2.1: Radiative and non-radiative energy transfer.

Fig. 2.2: Resonant and non-resonant energy transfer.

Fig. 2.3: Comparison of ETU (left) and ESA (right) upconversion.

---

[1]The terminology *donor* and *acceptor* is also being used in the literature.

[2]Auzel prefers to call it the *Auzel APTE effect*, for *addition de photon par transferts d'energie.*

Table 2.1: Typical efficiencies of different upconversion processes. The efficiencies are presented in the form of normalized values, assuming a two-photon process. Data are taken from [42].

Process	Material	Efficiency $\eta_{2\mathrm{p}}$ (cm^2/W)
ETU	YF$_3$:Yb:Er	10^{-3}
ESA	SrF$_2$:Er	10^{-5}
Cooperative sensitization	YF$_3$:Yb:Tb	10^{-6}
Cooperative luminescence	Yb:PO$_4$	10^{-8}
Second harmonic generation	KDP	10^{-11}
2-photon absorption	CaF$_2$:Eu^{2+}	10^{-13}

effect in semiconductors. This effect, which is not being described in detail here, is a result of cross-relaxation between ions and has a distinct threshold.

Efficiency and Power Dependence of the Upconverted Luminescence

The common way to define an efficiency is [40]

$$\eta = \frac{I(\omega_\mathrm{f})}{I(\omega_\mathrm{e})}, \tag{2.1}$$

where $I(\omega_\mathrm{f})$ is the fluorescence intensity and $I(\omega_\mathrm{e})$ is the excitation intensity. However, assuming a two-photon process, η is linearly dependent on the excitation itensity. Therefore, to get a quantity that is independent of excitation intensity, the two-photon efficiency is defined as the efficiency normalized with the excitation intensity,

$$\eta_{2\mathrm{p}} = \frac{I(\omega_\mathrm{f})}{I(\omega_\mathrm{e})^2}. \tag{2.2}$$

Note that the units of $\eta_{2\mathrm{p}}$ are cm^2/W. In table 2.1, the typical efficiencies in solid materials for different upconversion processes are listed. Different processes are usually present at the same time, but the values give a hint of their relative contribution.

Using low intensities that do not cause any saturation effects, the power dependence for all processes involving n photons, goes as P^n. Real upconverting systems can be very complex, involving a lot of intermediate steps, as will be seen in Section 2.4. Saturation often occur at some point in the process, modifying the power law which states that a process showing a power dependence P^n involves at least n photons. This has in many cases, for example, for the blue emission line in the Yb^{3+}–Tm^{3+}–pair, led to confusion. This line is a result of a three-photon-upconversion process, but has a quadratic power dependence due to saturation in an intermediate step.

2.2 A Simple Model — The Three Level System

It is quite easy to describe the upconversion processes using a simple model with rate equations. Here, the simplest possible case is considered, which is a two-photon upconversion process in a three-level system with resonant levels. The

number of electrons in different energy levels in both sensitizers and activators are treated as one quantity. Also, the following assumptions are made [45]:

1. Ground-state bleaching is negligible, i.e. the ground state population $N_0 = \text{const}$.

2. The system is pumped by countinous wave (CW) light, that excites the first level.

3. Upconversion is due to either ETU or ESA.

4. The excited states have lifetimes τ_1 and τ_2, respectively.

In the following, the two cases of ETU and ESA will be treated separately. It will be shown that both processes lead to a quadratic power dependence for the upconverted light under low pump powers, and a linear dependence for high pump powers. The power dependence of the reemitted light at the excitation wavelength will, however, differ.
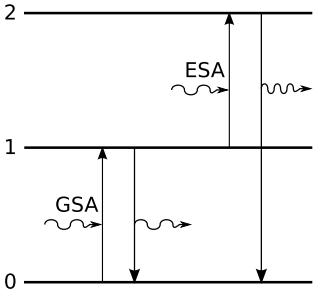
Power Dependance for ESA

Fig. 2.4: Three-level model for ESA upconversion.

The three-level model for ESA as the upconversion mechanism is shown in Fig. 2.4. The rate equations becomes

$$\frac{dN_1}{dt} = \rho\sigma_0 N_0 - \rho\sigma_1 N_1 - N_1/\tau_1, \tag{2.3}$$

$$\frac{dN_2}{dt} = \rho\sigma_1 N_1 - N_2/\tau_2, \tag{2.4}$$

where $\rho = \lambda I/hc$ is proportional to the pump power. σ_0 is the cross section for ground state absorption (GSA) and σ_1 for excited state absorption. In the steady-state case, it is always true that $N_2 \propto PN_1$. If the pump intensity is low, the ESA term (the second one on the right hand side of (2.3)) can be neglected, giving $N_1 \propto P$, because N_0 is treated as a constant. Together, this gives $N_2 \propto P^2$, implying that the power dependence of the upconverted light is quadratic while the power dependence of the light emitted at the excitation wavelength is linear.

On the other hand, if the pump power is strong, the spontaneous decay term in (2.3) can be neglected and $N_1 \propto N_0$, giving $N_2 \propto PN_1 \propto P$. Thus, for high pump powers, the upconverted light shows a linear power dependence while the intermediate level population N_1 is constant, as a result, the luminescence at the excitation wavelength becomes proportional to P.

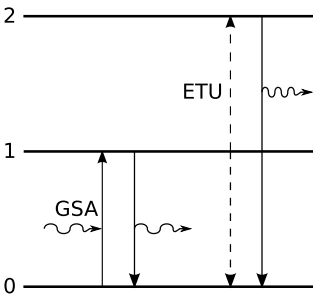### Power Dependance for ETU

Fig. 2.5: Three level model for ETU.

In Fig. 2.5, ETU is described in a three-level system. ETU is a process involving two ions being in the first excited state, and therefore, it is proportional to N_1^2. The rate equations become

$$\frac{dN_1}{dt} = \rho\sigma_0 N_0 - 2WN_1^2 - N_1/\tau_1, \tag{2.5}$$

$$\frac{dN_2}{dt} = WN_1^2 - N_2/\tau_2, \tag{2.6}$$

where W is a parameter describing the strength of the ETU process. For the steady-state solution, it follows from (2.6) that $N_2 \propto N_1^2$. If the pump power is low, the upconversion term in (2.5) can be neglected and $N_1 \propto P$. For N_2, this again gives $N_2 \propto P^2$, implying that the upconverted light shows a quadratic power dependence and the emitted light at the excitation wavelength shows a linear dependence.

For high pump powers, the upconversion term in (2.5) dominates over the spontaneous emission and $N_1 \propto P^{1/2}$. In this case, $N_2 \propto N_1^2 \propto P$, i.e. a linear power dependence for the upconverted light and a $P^{1/2}$-dependence for the emitted light at the excitation wavelength.

2.3 Nanosized Upconverting Crystals

The first nanosized upconverting particles presented were lanthanide doped oxides (Y_2O_3), mainly because those were easy to fabricate [46]. The focus has then been shifted towards fluorides because of their higher efficiencies. The higher efficiencies can be explained by the low phonon energies in fluorides, which lower the probability for non-radiative decay [47].

The material, which recently has gained increased interest, is sodium yttrium tetrafluoride ($NaYF_4$), co-doped with either Yb^{3+}/Er^{3+} or Yb^{3+}/Tm^{3+}. $NaYF_4$ can crystallize in two phases, cubic or hexagonal, called α-$NaYF_4$ and β-$NaYF_4$, respectively. The upconverted luminescence from the β-phase material is approximately one order of magnitude higher compared to the upconverted luminescence from the α-phase [48].

The luminescence from the nanosized particles is two to three magnitudes lower than from the bulk form of the crystals. This is mainly because of two factors. First, the particles crystallizes in the α phase with the fabrication methods used initially. Notice that currently, it is also possible to fabricate nanosized particles in the hexagonal phase [49]. Second, the particles contain small OH^--impurities, along with the fact that many Er^{3+} and Tm^{3+} pairs are situated close to the surface, causes them to be sensitive to quenching by the solvent. [18]

Disregarding the efficiency differences, the particles have also shown other interesting size-dependent properties. For example, the ratio between the different emission lines is different for nanoparticles and bulk material.

Bioimaging Applications

Because of their unique optical properties, upconverting nanoparticles have been proposed as biological markers for different bioimaging applications [19, 48, 46, 50]. There are cheap laser diodes at the excitation wavelength of 980 nm, which is a very suitable wavelength for bioimaging applications since the light penetrates relatively deep in tissue, which lowers the risk of photodamage. With Stokes-shifted fluorophores, the signal quality is usually limited by tissue autofluorescence. With upconverting nanocrystals, one will not suffer from any autofluorescence, hence giving the possibility to obtain better contrast.

To be able to use the particles *in vivo*, all particles have to be optically identical and biocompatible. Because of the size dependent optical properties of the particles, they must have a narrow size distribution [46]. The bare particles described above are not biocompatible since they are not soluble in

water.[3] In addition, the particles also need to be biofunctionalized, giving them for example tumor seeking abilities. The work for achieving this is under way in different research groups around the world.

Water Solubility

In order to obtain water soluble particles, they have to be given some polarity. A brief summary of some of the current employed methods is given below.

A straightforward way to make the particles water soluble is to coat the particles with a structure that is polar. The most widely used coatings are polymers and silica. Both synthetic polymers, for example, Polyethylene glycol (PEG), and natural polymers have been studied. It has been shown that these polymers are stable in biological environments and do not interfere with the optical properties of the nanocrystals in any significant negative way [51, 52, 53, 54]. Coating the particles with silica usually gives a slightly poorer water solubility compared to polymers. However, silica is very robust, which can be a very important factor to consider if the coated particles are used in biological environments [55, 56].

There are also reports of fabricating water soluble particles without coatings. Wang *et al.*, have shown that it is possible to attach hydroxyl groups to the surfaces of the particles either by chemical bonds or physical absorption [57]. Hydroxyl groups are by definition formed by covalent binding, and the final structure usually have polar properties. This method can unfortunately cause significant quenching effects of the luminescence via non-radiative decays. In addition, without a stable protective coating, they might not be as suitable in biological environments as their coated counterparts.

Functionalization

Functionalization of the upconverting nanoparticles is a hot field that is rapidly developing very much thanks to the experience and knowledge obtained from functionalizing quantum dots [14], where some methods are applicable on upconverting rare-earth doped nanoparticles. Early studies of functionalization of upconverting nanoparticles have been reported and the prospects are very promising [58, 59].

2.4   Particles Used in This Work

The particles used in this thesis were fabricated under a collaboration project by Harbin Institute of Technology. The particles were $NaYF_4$-crystals prepared according to the method described in [60], doped with a combination of Yb^{3+} and Tm^{3+}. The energy diagrams for the two ions are shown in Fig. 2.6. Figure 2.7 shows the emission spectrum for the nanoparticles, the blue emission line at 477 nm is only visisble for higher pump intensities. The pump-power dependence of the 800 nm line was measured to be quadratic using low intensities, as seen in the inset of Fig. 2.7.

---

[3]Although particles prepared with some methods can form transparent colloids in non-polar solvents.
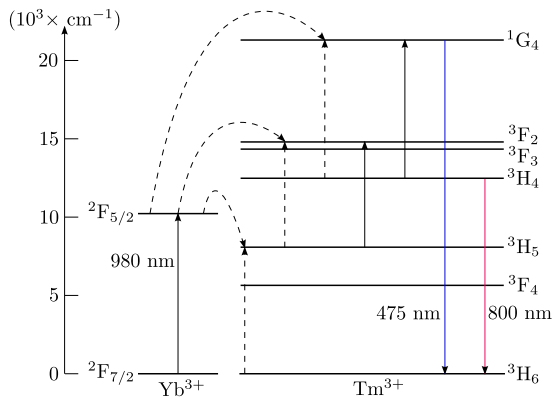
Fig. 2.6: Upconversion processes in the Yb^{3+}–Tm^{3+} ion pair. Non-radiative upconverting processes are illustrated with dashed arrows and non-radiative decays are omitted for clarity. The figure is drawn according to the results in [47, 61, 62].

Fig. 2.7: Emission spectrum recorded for the nanoparticles under 980 nm excitation with an intensity of 6 W/cm^2. The inset shows the pump-power dependence of the interesting 800 nm line measured under low intensities.

Optical Tomography

In two dimensional optical imaging, a picture is taken of the light distribution on the surface. This cannot resolve the depth or concentration of the fluorophore. Optical tomography aims at reconstructi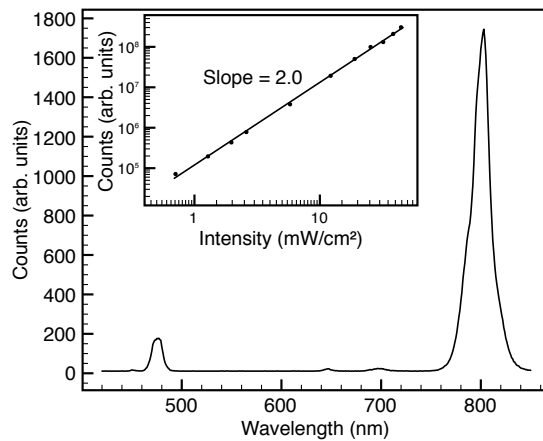ng the fluorophore distribution in three dimensions [63]. This is important, for instance, to monitor biological responses from drugs on cancer tumor over a period of time, without sacrificing the animals.

The procedure resembles those used for computed tomography (CT), but in contrast to X-rays, photons in the optical regime are highly scattered in tissue. The tissue usually needs to be illuminated at multiple positions and the signal is also collected at multiple positions.

The aim of optical tomography, in the general case, is to reconstruct the optical parameters in the RTE, μ_a and μ_s, in every pixel of the three dimensional domain. The measurement procedure can be described by a non-linear operator

$$\mathbf{y} = F(\mathbf{p}), \tag{3.1}$$

mapping the optical parameters in every point $p_{i,j} = (\mu_a, \mu_s)_{i,j}$ into the measurements, represented by a vector $\mathbf{y}$. The solution to the problem is then given by

$$\mathbf{p} = F^{-1}(\mathbf{y}). \tag{3.2}$$

To solve the inverse problem, different approaches have been investigated. The use of back-projection algorithms like those used in X-ray CT, have been proposed which as of today have not been successful. Perturbative methods, which linearize F around an initial guess, together with non-linear optimization methods, which seeks to repeatedly update and estimate the solution, have been the most promising approaches so far. It has been demonstrated that optical tomography, i.e. to find the parameters μ_a and μ_s in every point, is not possible in the steady-state case. To be able to decouple the two parameters, the measurements need to be performed in the time or frequency domain. [64, 65]

A special case of optical tomography is Fluorescence Molecular Tomography, (FMT). Here, fluorescent contrast agents are used, and the fluorescent yield, which is proportional to the concentration of the fluorophore, represents

the unknown. If reasonable approximations are introduced, the problem becomes linear. Also the fluorophore lifetime can be used as contrast, but this of course requires measurements in the time or frequency domain [66].

This chapter begins with derivations of some useful analytical solutions. Then, a model and necessary boundary conditions are introduced. The chapter ends with an overview of the computational methods used in optical tomography and a discussion of some issues arising when using fluorophores showing a quadratic power dependence.

3.1   Analytical Solutions for the Diffusion Approximation

In section 1.2, it was shown that under certain conditions, the Boltzmann equation can be approximated with the diffusion approximation. In some simple geometries, analytical solutions can be found. In the following section, the Green's function for an infinite homogenous medium is derived. From this function, also the Green's function for a semi-infinite medium, a slab and a sphere can be found using the technique of mirrored sources [1].

Even if realistic tissue is inhomogenous and does not have some of the simple geometries mentioned above, the analytical Green's function is a very useful tool for approximations and for efficient calculations.

Green's Function for the Diffusion Equation

For a homogenous medium, the diffusion equation is given by

$$\left(\frac{1}{c}\frac{\partial}{\partial t} + \mu_{\mathrm{a}} - \kappa \nabla^2 \right) \Phi(\mathbf{r}, t) = Q(\mathbf{r}, t), \tag{3.3}$$

where $\Phi(\mathbf{r}, t)$ is the fluence rate at point $\mathbf{r}$ at time t and $\kappa = 1/3(\mu_{\mathrm{s}}' + \mu_{\mathrm{a}})$ is the diffusion coefficient.[1] After a Fourier transform, the equation takes the simple form

$$\left(\frac{\mathrm{i}\omega}{c} + \mu_{\mathrm{a}} + \kappa |\mathbf{k}|^2 \right) \widetilde{\Phi}(\mathbf{k}, \omega) = \widetilde{Q}(\mathbf{k}, \omega). \tag{3.4}$$

To get the Green's function for a homogeneous infinite medium, the equation should be solved with the source term $Q(\mathbf{r}, t) = \delta(\mathbf{r} - \mathbf{y})\delta(t - s)$, or in the Fourier domain, $\widetilde{Q}(\mathbf{k}, \omega) = \mathrm{e}^{\mathrm{i}\mathbf{k}\cdot\mathbf{y}}\mathrm{e}^{-\mathrm{i}\omega s}$. From (3.4) it follows that

$$\widetilde{\Phi}(\mathbf{k}, \omega) = \frac{\mathrm{e}^{\mathrm{i}(\mathbf{k}\cdot\mathbf{r} - \omega s)}}{\mathrm{i}\omega/c + \mu_{\mathrm{a}} + \kappa |\mathbf{k}|^2}. \tag{3.5}$$

Taking the inverse transform gives

$$\Phi(\mathbf{r}, t) \quad = \quad \frac{1}{(2\pi)^4} \iint \widetilde{\Phi}(\mathbf{k}, \omega) \mathrm{e}^{\mathrm{i}(\mathbf{r}\cdot\mathbf{x} - \omega t)} \, \mathrm{d}^3\mathbf{k} \, \mathrm{d}\omega \tag{3.6}$$

$$= \quad \frac{1}{(2\pi)^4} \iint \frac{\mathrm{e}^{-\mathrm{i}(\mathbf{r}\cdot(\mathbf{x} - \mathbf{y}) - \omega(t - s))}}{\mathrm{i}\omega/c + \mu_{\mathrm{a}} + \kappa |\mathbf{k}|^2} \, \mathrm{d}^3\mathbf{k} \, \mathrm{d}\omega. \tag{3.7}$$

---

[1]The definition of κ is a well discussed topic. An alternative definition is $\kappa = 1/3\mu_{\mathrm{s}}'$. See section 1.2.

Writing $\xi = |\mathbf{r} - \mathbf{y}|$ and $\tau = t - s$, and changing to spherical coordiantes with $r = |\mathbf{k}|$, while noting that $\mathbf{k} \cdot (\mathbf{r} - \mathbf{y}) = r\xi \cos\theta$, the integral becomes

$$\Phi(\mathbf{r}, t) = \frac{1}{(2\pi)^4} \int_{-\infty}^{\infty} \int_{\Omega} \frac{e^{-i(r\xi \cos\theta - \omega\tau)}}{i\omega/c + \mu_{\mathrm{a}} + \kappa r^2} r^2 \sin\theta \, d\theta \, dr \, d\varphi \, d\omega, \qquad (3.8)$$

where Ω represents the whole $\mathbf{k}$-space. Carrying out the integration with respect to φ and θ leads to

$$
\begin{aligned}
\Phi(\mathbf{r}, t) &= \frac{1}{(2\pi)^3} \int \int_{\Omega} \frac{e^{-i(r\xi \cos\theta - \omega\tau)}}{i\omega/c + \mu_{\mathrm{a}} + \kappa r^2} r^2 \sin\theta \, d\theta \, dr \, d\omega && (3.9) \\
&= \frac{1}{(2\pi)^3} \int \int_{\Omega} \frac{r^2 e^{i\omega\tau}}{i\omega/c + \mu_{\mathrm{a}} + \kappa r^2} \left[\frac{e^{-ir\xi \cos\theta}}{ir\xi} \right]_{\theta=0}^{\pi} \, dr \, d\omega && (3.10) \\
&= \frac{1}{4\pi^3 \xi} \int_0^{\infty} r \sin(r\xi) \int_{-\infty}^{\infty} \frac{e^{i\omega\tau}}{i\omega/c + \mu_{\mathrm{a}} + \kappa r^2} \, d\omega \, dr. && (3.11)
\end{aligned}
$$

The ω-integral

The integral to solve is the complex integral

$$\int_{-\infty}^{\infty} \frac{e^{iz\tau}}{iz/c + \mu_{\mathrm{a}} + \kappa r^2} \, dz, \qquad (3.12)$$

along the real axis. The contour used is illustrated in Fig. 3.1. The function has a pole of first order at $z = ic(\mu_{\mathrm{a}} + \kappa r^2)$. The residue at the pole is $-ice^{-ic(\mu_{\mathrm{a}}+\kappa r^2)\tau}$, and the value of the integral is $2\pi c e^{-c(\mu_{\mathrm{a}}+\kappa r^2)\tau}$.[2]
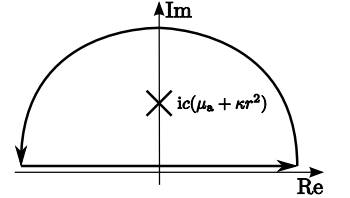

Fig. 3.1:   Integral contour used to solve (3.12).

The r-integral

Putting the result from the calculation of the ω-integral above into (3.11), leads to

$$\Phi(\mathbf{r}, t) = \frac{c}{2\pi^2 \xi} e^{-c\mu_{\mathrm{a}}\tau} \int_0^{\infty} r e^{-c\kappa\tau r^2} \sin(r\xi) \, dr. \qquad (3.13)$$

After some algebra, a primitive can be found,

$$
\int_0^{\infty} r \sin(r\xi) e^{-c\kappa\tau r^2} \, dr = \frac{1}{2i} \int_0^{\infty} r e^{-c\kappa\tau \left(r^2 - i\frac{\xi r}{c\kappa\tau}\right)} \, dr -
$$
$$
- \frac{1}{2i} \int_0^{\infty} r e^{-c\kappa\tau \left(r^2 + i\frac{\xi r}{c\kappa\tau}\right)} \, dr \qquad (3.14)
$$

Splitting up the exponent in two parts and introducing the new variable $u = (r - i\xi/2c\kappa\tau)\sqrt{c\kappa\tau}$ give

$$
\begin{aligned}
\int_0^{\infty} r e^{-c\kappa\tau \left(r^2 - i\xi r/c\kappa\tau\right)} &= \int_0^{\infty} r e^{-c\kappa\tau (r - i\xi r/2c\kappa\tau)^2} e^{-\xi^2/4c\kappa\tau} \, dr = \\
&= \frac{e^{-\xi^2/4c\kappa\tau}}{\sqrt{c\kappa\tau}} \int_0^{\infty} \left(\frac{u}{\sqrt{c\kappa\tau}} + i\frac{\xi}{2c\kappa\tau} \right) e^{-u^2} \, du = \\
&= \frac{e^{-\xi^2/4c\kappa\tau}}{\sqrt{c\kappa\tau}} \left(\frac{2}{\sqrt{c\kappa\tau}} + i\frac{\xi\sqrt{\pi}}{4c\kappa\tau} \right), \qquad (3.15)
\end{aligned}
$$

---

[2]That the integral along the contour around the upper half plane becomes zero is guaranteed by Jordan's lemma.

and the same with opposite sign on the imaginary part for the second term in (3.14). The r-integral eventually becomes

$$\int_0^\infty r \sin(r\xi) e^{-c\kappa\tau r^2} \, \mathrm{d}r = \sqrt{\frac{\pi}{(c\kappa\tau)^3}} \frac{\xi}{4} e^{-\xi^2/4c\kappa\tau}. \tag{3.16}$$

Putting this result into (3.13) the Green's function is finally given by

$$\Phi(\mathbf{r}, t; \mathbf{y}, s) = \frac{1}{8\sqrt{(\pi\kappa\tau)^3 c}} e^{-\xi^2/4c\kappa\tau} e^{-c\mu_\mathrm{a}\tau}, \tag{3.17}$$

with $\xi = |\mathbf{r} - \mathbf{y}|$ and $\tau = t - s$.

Steady-state Green's Function

For the steady-state case, the time derivative equals zero, and (3.3) becomes

$$\left(\mu_\mathrm{a} - \kappa\nabla^2\right)\Phi(\mathbf{r}) = Q(\mathbf{r}). \tag{3.18}$$

To get the Green's function, the right hand side should be $Q(\mathbf{r}) = \delta(\mathbf{r} - \mathbf{y})$. In the Fourier domain, the equation is

$$\left(\mu_\mathrm{a} + \kappa\nabla^2\right)\widetilde{\Phi}(\mathbf{k}) = e^{i\mathbf{k}\cdot\mathbf{r}}. \tag{3.19}$$

The solution in the Fourier domain is

$$\widetilde{\Phi}(\mathbf{k}) = \frac{e^{i\mathbf{k}\cdot\mathbf{r}}}{\mu_\mathrm{a} + \kappa|\mathbf{k}|^2}. \tag{3.20}$$

Taking the inverse transform gives

$$\Phi(\mathbf{r}) = \frac{1}{(2\pi)^3} \int_\Omega \frac{e^{-i\mathbf{k}\cdot(\mathbf{r}-\mathbf{y})}}{\mu_\mathrm{a} + \kappa|\mathbf{k}|^2} \, \mathrm{d}^3\mathbf{k}. \tag{3.21}$$

A change to spherical coordinates, noting that $\mathbf{k} \cdot (\mathbf{r} - \mathbf{y}) = r\xi\cos\theta$, with $r = |\mathbf{k}|$ and $\xi = |\mathbf{r} - \mathbf{y}|$, gives

$$\Phi(\mathbf{r}) = \frac{1}{(2\pi)^3} \int_\Omega \frac{e^{-ir\xi\cos\theta}}{\mu_\mathrm{a} + \kappa r^2} r^2 \sin\theta \, \mathrm{d}r \, \mathrm{d}\theta \, \mathrm{d}\varphi \tag{3.22}$$

$$= \frac{1}{(2\pi)^2} \int_0^\infty \frac{r^2}{\mu_\mathrm{a} + \kappa r^2} \int_0^\pi e^{-ir\xi\cos\theta} \sin\theta \, \mathrm{d}\theta \, \mathrm{d}r. \tag{3.23}$$

The θ-integral can be solved simply by using the primitive function,

$$\int_0^\infty e^{-ir\xi\cos\theta} \sin\theta \, \mathrm{d}\theta = \left[\frac{e^{-ir\xi\cos\theta}}{ir\xi}\right]_{\theta=0}^\pi = 2\sin(r\xi)/r\xi. \tag{3.24}$$

Putting the result into (3.23) gives

$$\Phi(\mathbf{r}) = \frac{1}{2\pi^2\xi} \int_0^\infty \frac{r}{\mu_\mathrm{a} + \kappa r^2} \sin(r\xi) \, \mathrm{d}r = \frac{1}{4\pi^2\xi} \int_{-\infty}^\infty \frac{r}{\mu_\mathrm{a} + \kappa r^2} \sin(r\xi) \, \mathrm{d}r, \tag{3.25}$$

where the last equality follows from the function being even.

It is easier to solve the complex integral

$$\int_{-\infty}^{\infty} \frac{z \mathrm{e}^{\mathrm{i}z\xi}}{\mu_{\mathrm{a}} + \kappa z^2} \, \mathrm{d}z, \tag{3.26}$$

along the real axis, whose imaginary part is proportional to (3.25). Taking the countur around the upper half of the complex plane, see Fig. 3.2, noting that the integrand has a pole in $z = \mathrm{i}\sqrt{\mu_{\mathrm{a}}/\kappa}$, the integral gets the value[3]

$$2\pi\mathrm{i} \frac{\mathrm{e}^{-\xi\sqrt{\mu_{\mathrm{a}}/\kappa}}}{2\kappa}. \tag{3.27}$$

Putting the imaginary part into (3.25) eventually gives the Green's function as

$$\Phi(\mathbf{r}; \mathbf{y}) = \frac{1}{4\pi\kappa\xi} \mathrm{e}^{-\mu_{\mathrm{eff}}\xi}, \tag{3.28}$$

with $\mu_{\mathrm{eff}} = \sqrt{\mu_{\mathrm{a}}/\kappa}$.

Fig. 3.2: Integral contour used to solve (3.26).

3.2 Boundary Conditions

How to apply the correct boundary conditions is a non-trivial topic. In the RTE, the boundary condition states that photons exiting the boundary are lost. This condition can not be completely fulfilled by the diffusion equation. Instead, it is assumed that the total amount of inward-travelling fluence current should be zero [67],

$$\int_{\hat{\mathbf{s}} \cdot \hat{\mathbf{n}} < 0} \hat{\mathbf{s}} \phi(\mathbf{r}, \hat{\mathbf{s}}, t) \, \mathrm{d}\Omega = 0 \ , \ \mathbf{r} \in \partial\Omega, \tag{3.29}$$

which eventually leads to the Robin conditions

$$\Phi(\mathbf{r}) + 2\kappa(\mathbf{r})\hat{\mathbf{n}} \cdot \nabla\Phi(\mathbf{r}) = 0 \ , \ \mathbf{r} \in \partial\Omega. \tag{3.30}$$

Equation (3.30) only holds if there are no diffuse reflections from the surface. To account for the diffuse reflectance, Groenhuis *et al.* [68] suggest to let the total inward-travelling photon current be equal to the total outward-travelling photon current weighted by a reflection factor A

$$\int_{\hat{\mathbf{s}} \cdot \hat{\mathbf{n}} < 0} \hat{\mathbf{s}} \phi(\mathbf{r}, \hat{\mathbf{s}}, t) \, \mathrm{d}\Omega = \int_{\hat{\mathbf{s}} \cdot \hat{\mathbf{n}} > 0} A(\hat{\mathbf{s}}) \hat{\mathbf{s}} \Phi(\mathbf{r}, \hat{\mathbf{s}}, t) \, \mathrm{d}\Omega \ , \ \mathbf{r} \in \partial\Omega, \tag{3.31}$$

which leads to

$$\Phi(\mathbf{r}) + 2A\kappa(\mathbf{r})\hat{\mathbf{n}} \cdot \nabla\Phi(\mathbf{r}) = 0 \ , \ \mathbf{r} \in \partial\Omega. \tag{3.32}$$

Using Fresnel's law, A can be expressed as

$$A = \frac{2/(1 - R_0) - 1 + |\cos\theta_c|^3}{1 - |\cos\theta_c|^2}, \tag{3.33}$$

where θ_c is the critical angle for total internal reflection. The above equation has been justified through comparisons with Monte Carlo simulations [69].

---

[3]The convergence of the integral along the upper contour can also here be guaranteed according to Jordan's lemma.
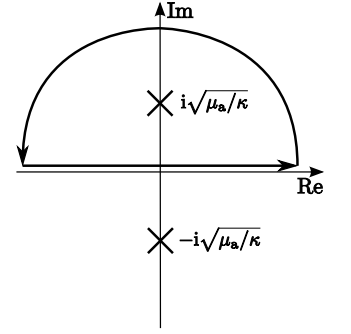
3.3   The Forward Model

In the diffusion approximation, the excitation field is determined by the diffusion equation,[4]

$$\left(\mu_a^e - \kappa_e \nabla^2\right) \Phi_e(\mathbf{r}) = S(\mathbf{r}), \tag{3.34}$$

where μ_a^e and κ_e is the absorption coefficient and diffusion coefficient for the excitation wavelength, respectively. $S(\mathbf{r})$ is a source function, in this case describing the power density of the light source. The fluorescence field is governed by the same diffusion equation, only with different coefficients, due to the different optical properties at the different wavelength,

$$\left(\mu_a^f - \kappa_f \nabla^2\right) \Phi_f(\mathbf{r}) = n(\mathbf{r}) S_f\left[\Phi_e(\mathbf{r})\right]. \tag{3.35}$$

Here, $n(\mathbf{r})$ is the fluorophore number density, and $S_f\left[\Phi_e(\mathbf{r})\right]$ is a function describing how the fluorescence depends on the excitation field. For ordinary organic fluorophores, $S_f\left[\Phi_e(\mathbf{r})\right] = \eta\sigma\Phi_e(\mathbf{r})$, η denoting the fluorophore quantum yield and σ the absorption cross section at the excitation wavelength, thus the relation is linear [70].

   The upconverting nanoparticles have a non-linear power dependance, due to more than one photon being involved in the upconversion process, see chapter 2. The function is rather of the form $S_f\left[\Phi_e(\mathbf{r})\right] = C\left(\Phi_e(\mathbf{r})\right)^\gamma$, where C is a constant describing the upconversion efficiency of the particles, and γ determines the power dependance.[5]

   All together the problem is described by a system of two coupled differential equations,

$$\left(\mu_a^e - \kappa_e \nabla^2\right) \Phi_e(\mathbf{r}) = S(\mathbf{r}), \tag{3.36}$$
$$\left(\mu_a^f - \kappa_f \nabla^2\right) \Phi_f(\mathbf{r}) = n(\mathbf{r}) C \Phi_e(\mathbf{r})^\gamma. \tag{3.37}$$

The system is linear in the fluorophore number density, $n(\mathbf{r})$. The solution to the system can be expressed as

$$\Phi_e(\mathbf{r}) = \int_\Omega G_e(\mathbf{r}, \mathbf{r}') S(\mathbf{r}') \, \mathrm{d}^3 \mathbf{r}', \tag{3.38}$$

$$\Phi_f(\mathbf{r}) = \int_\Omega G_f(\mathbf{r}, \mathbf{r}') n(\mathbf{r}') C \Phi_e(\mathbf{r}')^\gamma \, \mathrm{d}^3 \mathbf{r}', \tag{3.39}$$

where $G_e(\mathbf{r}, \mathbf{r}')$ and $G_f(\mathbf{r}, \mathbf{r}')$ are the Green's functions for the first and second equation, respectively.

Detected Quantity   In non-invasive measurements, only photons exiting the boundary will be detected, which can be expressed as

$$\Gamma(\mathbf{r}) = -\kappa(\mathbf{r})\hat{\mathbf{n}} \cdot \nabla \Phi_f(\mathbf{r}) = \frac{1}{2A} \Phi_f(\mathbf{r}), \ \mathbf{r} \in \partial\Omega, \tag{3.40}$$

where the boundary condition in (3.32) has been used.

---

[4]In this equation, the absorption of the fluorophores has been neglected on the right hand side. The change in total absorption caused by the fluorophores can be considered to be small. This approximation is referred to as the *first Born approximation*.

[5]For the particles used in this thesis under the intensities obtainable in scattering medium, $\gamma \approx 2.0$, derived experimentally.

The Light Source In many applications, the light source is modeled as an isotropic point source at the distance $1/\mu_{\mathrm{s}}'$ from the boundary, where the first scattering event occurs.

A more realistic model could use a source of exponential decay in the direction of the incoming light,

$$S(\mathbf{r}) = S_0 \mu_{\mathrm{s}}' \mathrm{e}^{-\mu_{\mathrm{tr}}|z - z_s|} \delta(x - x_{\mathrm{s}}, y - y_{\mathrm{s}}), \tag{3.41}$$

for a source of strength S_0 at position $\mathbf{r}_{\mathrm{s}} = (x_{\mathrm{s}}, y_{\mathrm{s}}, z_{\mathrm{s}})$.

3.4 The Inverse Problem

The inverse model aims to find $n(\mathbf{r})$ in (3.39) given measurements of the fluorescent field, and in some cases, also the excitation field. This can be achieved by calculating the sensitivity profiles from every source-detector pair, via the emission light from a fluorophore, and finding the most likely fluorophore distribution. The problem can hence be formulated as an optimization problem which will be further discussed below.

Normalized Approach

Until now, all quantities discussed have been expressed in absolute values. In an experimental setup, coupling the measured quantities to the absolute quantities will always be a problem. In this section, it is shown that measuring also the excitation light at the detector positions can help to solve some of these problems.

With a detector, for example a charge-coupled-device (CCD) camera, the signal Θ_{d} is proportional to the amount of light that exits the phantom,

$$\Theta_{\mathrm{f}} = C_{\mathrm{d}} \Gamma_{\mathrm{f}}(\mathbf{r}_{\mathrm{d}}), \tag{3.42}$$

where C_{d} is a coupling constant. A laser beam of power P_{s}, creates a source of strength $S_0 = C_{\mathrm{s}} P_{\mathrm{s}}$. Assuming a point source at position $\mathbf{r}_{\mathrm{s}}$, the expression for the detected excitation light at position $\mathbf{r}_{\mathrm{d}}$ is

$$\Theta_{\mathrm{e}} = C_{\mathrm{d}} \Gamma_{\mathrm{e}}(\mathbf{r}_{\mathrm{d}}) = \frac{C_{\mathrm{d}} C_{\mathrm{s}} P_{\mathrm{s}}}{2A} G_{\mathrm{e}}(\mathbf{r}_{\mathrm{d}}, \mathbf{r}_{\mathrm{s}}). \tag{3.43}$$

Using this together with (3.39) and (3.40) in (3.42) gives

$$\Theta_{\mathrm{f}} = \frac{C_{\mathrm{d}} (C_{\mathrm{s}} P_{\mathrm{s}})^{\gamma}}{2A} \int_{\Omega} G_{\mathrm{f}}(\mathbf{r}_{\mathrm{d}}, \mathbf{r}') n(\mathbf{r}') G_{\mathrm{e}}(\mathbf{r}', \mathbf{r}_{\mathrm{s}})^{\gamma} \, \mathrm{d}^3 \mathbf{r}'. \tag{3.44}$$

The data function for a source-detector pair is then defined as [6]

$$D(\mathbf{r}_{\mathrm{d}}, \mathbf{r}_{\mathrm{s}}) = \frac{G_{\mathrm{e}}(\mathbf{r}_{\mathrm{d}}, \mathbf{r}_{\mathrm{s}})}{(C_{\mathrm{s}} P_{\mathrm{s}})^{\gamma - 1}} \times \frac{\Theta_{\mathrm{f}}}{\Theta_{\mathrm{e}}}. \tag{3.45}$$

---

[6] The choice to normalize with the excitation field is not obvious. For ordinary fluorophores with $\gamma = 1$, a normalization of the excitation field will make all the coupling constants disappear. In the case with $\gamma \neq 1$, it will make the coupling constants on the detector side disappear.

From (3.44) and (3.43), the final equation can be written

$$D(\mathbf{r}_\mathrm{d}, \mathbf{r}_\mathrm{s}) = \int_\Omega G_\mathrm{f}(\mathbf{r}_\mathrm{d}, \mathbf{r}') n(\mathbf{r}') G_\mathrm{e}(\mathbf{r}', \mathbf{r}_\mathrm{s})^\gamma \, \mathrm{d}^3 \mathbf{r}'. \qquad (3.46)$$

All Green's functions here can be calculated, analytically or numerically, and the two quantities Θ_f and Θ_e represent the measurements. The laser power P_s can easily be determined and the only nuisance is the coupling constant C_s, which in a simple experimental setup has approximately the same value for all source positions.

Discretization of the Problem

To solve equation (3.46) for the unknown quantity $n(\mathbf{r})$, the equation needs to be discretized. If the domain Ω is discretized into N_voxels voxels, the integral can be written as a sum,

$$D(\mathbf{r}_\mathrm{d}, \mathbf{r}_\mathrm{s}) = \sum_{i=1}^{N_\mathrm{voxels}} G_\mathrm{f}(\mathbf{r}_\mathrm{d}, \mathbf{r}_i) n(\mathbf{r}_i) G_\mathrm{e}(\mathbf{r}_i, \mathbf{r}_\mathrm{s})^\gamma \delta V_i, \qquad (3.47)$$

where δV_i is the volume of voxel i. Each source-detector pair gives rise to an equation of the form of (3.47), forming a system of equations that can be written in the matrix form,

$$\underbrace{\begin{bmatrix} J_{11} & J_{12} & \ldots & J_{1N_\mathrm{voxels}} \\ J_{21} & J_{22} & \ldots & J_{2N_\mathrm{voxels}} \\ \vdots & \vdots & & \vdots \\ J_{N_\mathrm{eq}1} & J_{N_\mathrm{eq}2} & \ldots & J_{N_\mathrm{eq}N_\mathrm{voxels}} \end{bmatrix}}_{\mathbf{J}} \underbrace{\begin{bmatrix} n(\mathbf{r}_1) \\ n(\mathbf{r}_2) \\ \vdots \\ n(\mathbf{r}_{N_\mathrm{voxels}}) \end{bmatrix}}_{\boldsymbol{\delta}} = \underbrace{\begin{bmatrix} D_1 \\ D_2 \\ \vdots \\ D_{N_\mathrm{eq}} \end{bmatrix}}_{\boldsymbol{\Phi}}. \qquad (3.48)$$

The matrix elements of $\mathbf{J}$ are of the form

$$J_{ni} = G_\mathrm{f}(\mathbf{r}_\mathrm{d}, \mathbf{r}_i) G_\mathrm{e}(\mathbf{r}_i, \mathbf{r}_\mathrm{s})^\gamma \delta V_i, \qquad (3.49)$$

and represents the n:th source-detector pair, and the elements in $\boldsymbol{\Phi}$ are the functions $D(\mathbf{r}_\mathrm{d}, \mathbf{r}_\mathrm{s})$, defined in (3.45), for the n:th source-detector pair.

Computational Method

In most cases, (3.48) is underdetermined and a unique solution cannot be found. However, by including additional information to the problem, $\boldsymbol{\delta}$ can still be computed. This process is called regularization. In the case for the diffusion equation, the solution is expected to be smooth, which can be seen as additional information to the problem.

A more straightforward way of dealing with the ill-posedness is to acquire more information by performing more measurements, which means to sacrifice time to improve ill-posedness. Since the problem is usually quite time consuming, a fast algorithm would be required for the calculations. By using various symmetry relations to develop fast inversion algorithms, Panasyuk *et al.* have shown experimentally that the ill-posedness can be partially alleviated by using very large data sets, i.e. $\geq 10^7$ independent measurements [70, 71].

Computing the quantities needed to solve the inverse problem in the forward model can be done in a variety of ways. Two popular methods are the finite element method (FEM) and the finite difference method (FDM) [35]. In this thesis, the FEM was chosen to solve the diffusion equation for the forward model. FEM is a numerical method well suited for approximating solutions to elliptic partial differential equations by discretizing the domain into a finite number of elements. On each element, the solution is approximated by a polynomial function. A full description of the FEM formulation is beyond the scope of this thesis, and the interested reader could, for example, consult [72, 73].

The goal in fluorescence tomography is to find the absorption or number density of the fluorophore in every voxel. More precisely, this means to minimize the differences between the measured Θ_f^m and the calculated Θ_f^c at the surfaces by adjusting the spatial distribution of the fluorophores inside the object of interest. Note that the minimization procedure aims at finding an approximate inverse to (3.48). Since the fluorophore concentration is linear with the absorption, by knowing the source term Θ_e^c for the fluorophores, the objective function which is to be minimized can be expressed as [74]

$$\chi^2 = \sum_{i=1}^{M} \left(\Theta_{f_i}^c(\mathbf{n}) - \Theta_{f_i}^m \right)^2 = \sum_{i=1}^{M} R_i^2(\mathbf{n}) = \|\mathbf{R}(\mathbf{n})\|^2, \qquad (3.50)$$

where M is the total number of measurements, $\mathbf{n} = (n_1, n_2, \ldots, n_N)$ is the input vector containing information about the fluorophore distribution, and the residuals R_i are introduced to make matter easier. The minimum of the objective function can be found by solving[7]

$$\nabla \chi^2 = 0. \qquad (3.51)$$

Taylor expanding $\nabla \chi^2$ and neglecting higher order terms around some initial fluorophore distribution guess, $\mathbf{n}^0$, give

$$\nabla \chi^2 \approx \nabla \chi^2 \left(\mathbf{n}^0 \right) - \mathbf{h} \cdot \nabla^2 \chi^2 \left(\mathbf{n}^0 \right), \qquad (3.52)$$

where $\mathbf{h} = \mathbf{n}^0 - \mathbf{n}$. Writing $\nabla \chi^2 = 0$ with the Taylor expanded expression and rearranging lead to

$$\mathbf{h} \cdot \nabla^2 \chi^2 \left(\mathbf{n}^0 \right) = \nabla \chi^2 \left(\mathbf{n}^0 \right). \qquad (3.53)$$

Introducing the Jacobian matrix,

$$\mathbf{J} = \begin{bmatrix} \frac{\partial R_1}{\partial n_1} & \frac{\partial R_1}{\partial n_2} & \cdots & \frac{\partial R_1}{\partial n_N} \\ \frac{\partial R_2}{\partial n_1} & \frac{\partial R_2}{\partial n_2} & \cdots & \frac{\partial R_2}{\partial n_N} \\ \vdots & \vdots & & \vdots \\ \frac{\partial R_M}{\partial n_1} & \frac{\partial R_M}{\partial n_2} & \cdots & \frac{\partial R_M}{\partial n_N} \end{bmatrix}, \qquad (3.54)$$

---

[7]Solving $\nabla \chi^2 = 0$ to minimize χ^2 essentially means to use Newton's optimization method instead of gradient descent method. Provided that the initial guess is somewhat close to the solution, this should give a faster convergence. It can be realized by, for example, considering how the parameters are updated at each iteration. Using gradient descent, the parameter will typically be updated as $\mu_x^{k+1} = \mu_x^k - \delta \nabla \chi^2$, meaning *smaller* steps where the gradient is *small* and *larger* steps where the gradient is *large*, which is exactly the opposite of what is wanted for a 'healthy' iteration method. Furthermore, gradient descent does not take the curvature difference for different directions into account. For example, for a long narrow valley, one should move with large steps along the base of the valley, and small steps in the directions of the walls. However, gradient descent will result in more motion in the directions of the walls than along the base.

and the Hessian matrix which is approximated by $\mathbf{H} \approx 2\mathbf{J}^T\mathbf{J}$, (3.53) can be rewritten in a more compact form

$$\mathbf{J}^T\mathbf{J}\mathbf{h} = \mathbf{J}^T\mathbf{R} = \mathbf{J}^T \left(\mathbf{\Theta}_f^c - \mathbf{\Theta}_f^m\right), \tag{3.55}$$

since

$$\nabla\chi^2 = 2\mathbf{J}^T\mathbf{R}. \tag{3.56}$$

Levenberg proposed to introduce a damping factor,[8] λ, which originally was meant to be tunable to bring the algorithm closer to gradient descent for big λ, and Gauss-Newton for small λ. Equation (3.55) now becomes

$$(\mathbf{J}^T\mathbf{J} + \lambda\mathbf{I})\mathbf{h} = \mathbf{J}^T \left(\mathbf{\Theta}_f^c - \mathbf{\Theta}_f^m\right). \tag{3.57}$$

$\mathbf{h}$ can now be updated for every iteration by repeatedly solving

$$\mathbf{h} = (\mathbf{J}^T\mathbf{J} + \lambda\mathbf{I})^{-1}\mathbf{J}^T \left(\mathbf{\Theta}_f^c - \mathbf{\Theta}_f^m\right). \tag{3.58}$$

Depending on the convergence rate, λ can be adjusted on each iteration until a satisfactory result is obtained.

If λ is large, the Hessian matrix $\mathbf{J}^T\mathbf{J}$ might have a very small contribution. Marquardt provided the insight to replace $\mathbf{I}$ with the diagonal of the Hessian matrix, i.e.

$$\mathbf{h} = (\mathbf{J}^T\mathbf{J} + \lambda \cdot \text{diag}(\mathbf{J}^T\mathbf{J}))^{-1}\mathbf{J}^T \left(\mathbf{\Theta}_f^c - \mathbf{\Theta}_f^m\right), \tag{3.59}$$

which can be seen as a scaling factor to ensure good step sizes. Note that the Moore-Penrose inverse,

$$(\mathbf{J}^T\mathbf{J} + \lambda\mathbf{I})^{-1}\mathbf{h} = \mathbf{J}^T(\mathbf{J}\mathbf{J}^T + \lambda\mathbf{I})^{-1}, \tag{3.60}$$

can be identified in (3.58), which has been shown to be highly suitable for underdetermined systems [75].

---

[8]Which really is the regularization factor here [74, 35], since it is used in helping to solve ill-posed problems.

4

Experimental

To determine whether or not upconverting nanocrystals could be used as a fluorophore for *in vivo* applications, two studies were performed in this thesis. Section 4.1 demonstrates the differences in contrast using traditional downconverting fluorophores and upconverting nanocrystals and is largely based on the work presented in [76]. Section 4.2 demonstrates the simulations performed for tomographic reconstruction using upconverting nanocrystals.

The systems used for data collection are shown schematically in Fig. 4.1. The tissue phantom consisted of a solution of intralipid and ink with optical properties determined by a time-of-flight spectroscopy system [77]. The fluorophores were contained in capillary tubes with inner diameters of 2.4 mm. The concentrations of the fluorophores were 1 wt% for the nanoparticles and 1 μM for the DY-781. The concentration of the nanoparticles was chosen to have a reasonable correspondence with studies using quantum dots [14, 13]. In those studies, approximately 1 nmol of CdSe quantum dots were injected into a mouse ($\sim$ 18 g). If the quantum dots are distributed homogeneously in mice, it would give a weight concentration of approximately 0.01 wt%. In a realistic case, functionalized quantum dots would be used, giving a selective tumor accumulation. Since the nanoparticles have molar mass of the same order of magnitude as the quantum dots, the concentration of 1 wt% used in this thesis seems acceptable.

Using two step motors from a CNC machine, the fiber coupled lasers could be raster scanned. An image was acquired for each scanned position with an air cooled CCD camera sitting behind two dielectric bandpass filters centered at 800 nm.

4.1 Autofluorescence Insensitive Fluorescence Molecular Imaging

An epi-fluorescence setup was used for this study. The optical properties of the phantom was chosen to be $\mu'_s = 6.5$ cm^{-1} and $\mu_a = 0.44$ cm^{-1} at 660 nm, which fall into the range of those found in small animals [78, 5]. The capillary tubes containing the fluorophores, DY-781 and NaYF$_4$:Yb^{3+}/Tm^{3+}, were submerged
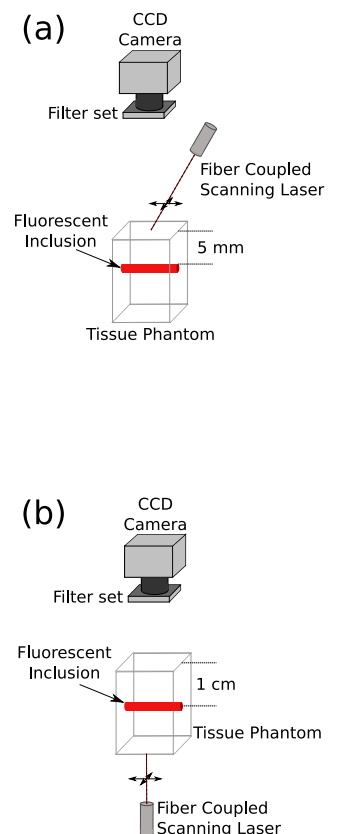
Fig. 4.1: (a) The setup used for fluorophore imaging (epi-fluorescence). (b) The thought setup used for fluorophore reconstruction (transillumination).

to a depth of 5 mm, where the depth was taken as the distance from the front surface of the tubes to the surface of the phantom. DY-781 was chosen in order to get a fair comparison, since it emits at 800 nm too and has a quantum efficiency *on par* with more commonly used dyes, for example the rhodamine class. Two diode lasers were used to excite the fluorophores. DY-781 was excited at 780 nm, and the nanoparticles were excited at 980 nm. The lasers were raster scanned over an area of 4.4×4.4 cm^2 consisting of 121 positions. The images were then summed, giving a representation of the photon distribution on the surface. This, however, does not accurately reflect the internal fluorophore distribution, but it provides an idea of whether or not a fluorescent inclusion can be detected. In order to suppress the effects of bad pixels on the camera, a median filter with a kernel of 3×3 pixels was applied to the summed images. To simulate autofluorescence, DY-781 was added into the phantom up to a point where the contrast was so poor that the data could not be used in a sensible way.

Since the main idea behind this study is to determine whether or not the nanoparticles can be used for a realistic case, it was important to use intensities that were deemed non-harmful to tissue. The final used excitation light had a spot size of 1 cm^2 from both lasers on the surface of the phantom, giving intensities of 40 mW/cm^2 for the 780 nm laser and 85 mW/cm^2 for the 980 nm laser. Figure 4.2 shows the images taken with and without autofluorescence along with their cross section profiles. The figure clearly demonstrates the contrast difference using downconverting and upconverting fluorophores. It is worth to notice that even without any artificial autofluorophores added, the intralipid itself autofluoresces and the effect is visible in the cross section profile in Fig. 4.2 (a). For demonstration purposes, two raw images using the two different fluorophores without any added autofluorophores acquired at the same position are shown in Fig. 4.3, which further emphasizes the autofluorescence issue.

As mentioned and seen in Fig. 4.2, the signal-to-background contrast is superior for the upconverting nanoparticles. The end result using the nanoparticles is mainly limited by the signal-to-noise ratio of the detector. This means that by increasing the excitation power, it is possible to enhance the obtainable image quality. The situation is different for the DY-781 dye. The dye is very efficient, and is in general not limited by the signal-to-noise ratio. However, as seen in Fig. 4.2, it is limited by the signal-to-background contrast. This means that an increase in excitation power will not result in a better image quality.

4.2   Fluorescence Molecular Tomography

Simulations of FMT using upconverting nanoparticles and traditional fluorophores were performed in transmission-fluorescence setups. The simulated tissue phantom was modeled as a $80 \times 80 \times 20$ mm^3 slab with $\mu'_s = 6.5$ cm^{-1} and $\mu_a = 0.25$ cm^{-1} at $\lambda = 660$ nm, with 100 uniformly spaced sources and 100 uniformly spaced detectors. The fluorophores were placed in $2.4 \times 80 \times 2.4$ mm^3 rectangular stick extending throughout the phantom at a depth of 10 mm as shown in Fig. 4.1 (b). The forward model used a uniform mesh consisting of 29449 nodes, see Fig. 4.4. For the reconstructions, a pixel basis of
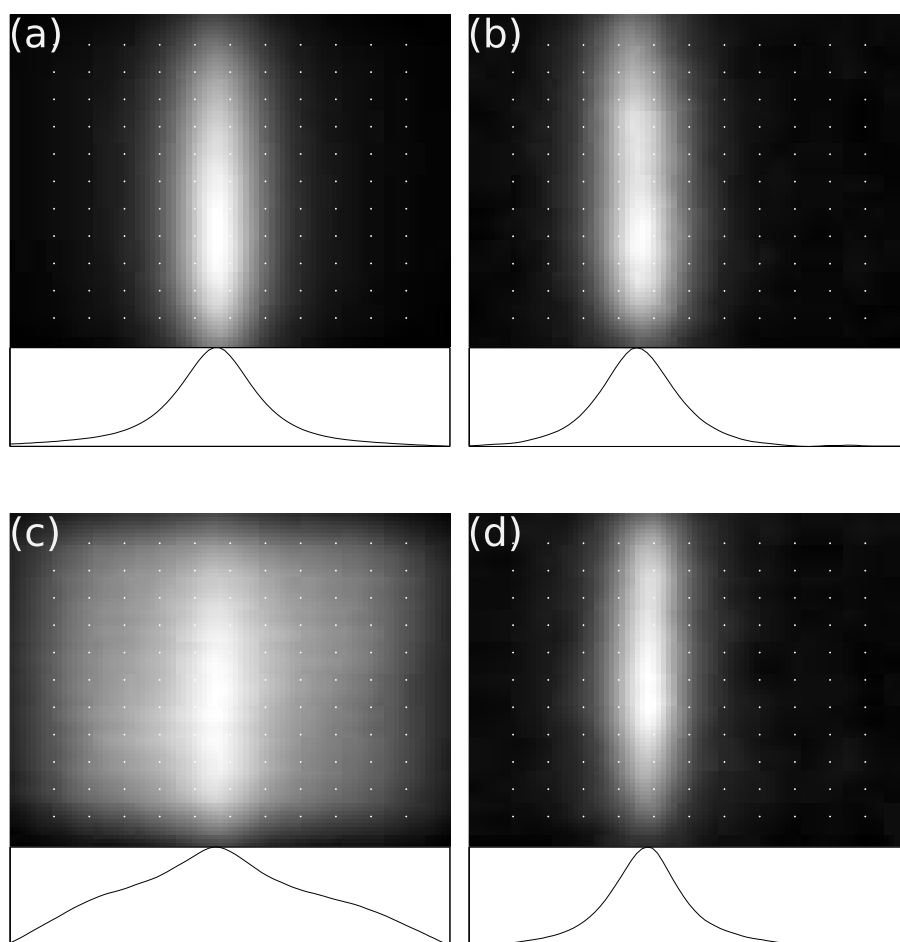
Fig. 4.2: Images comparing the DY-781 dye and the nanoparticles with and without autofluorescence, along with plots showing the sums in the vertical directions. The white dots have been added artificially and represent the positions used for the excitation light. The left column shows the results using DY-781, and the right column shows the results using upconverting nanoparticles. (a) and (b) are taken without any added autofluorophores. (c) and (d) are taken with a background autofluorophore concentration of 40 nM.
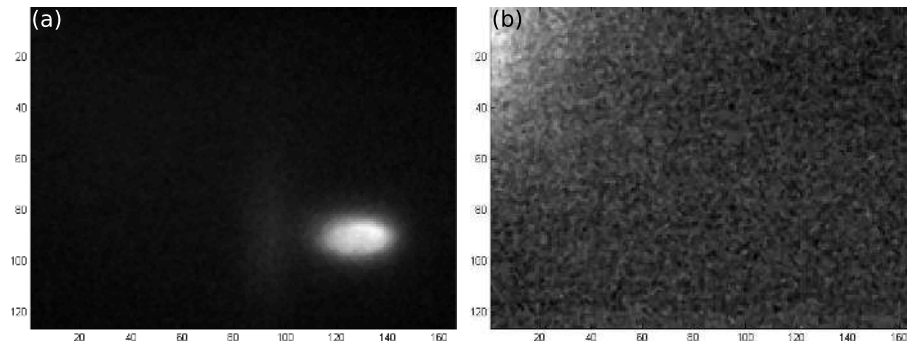
Fig. 4.3: Raw images from the measurements performed in [76]. The scale differs in the two images and is normalized to the peak intensities. (a) Raw image showing the autofluorescence from a phantom without any added autofluorophores. (b) Raw image from the same setup using upconverting nanocrystals where only the noise is visible.

Fig. 4.4: A $80 \times 80 \times 20$ mm^3 slab used for simulating the forward data. The mesh consisted of 29449 nodes. The source and the detector positions have been marked as well, showing 100 uniformly spaced sources and detectors.
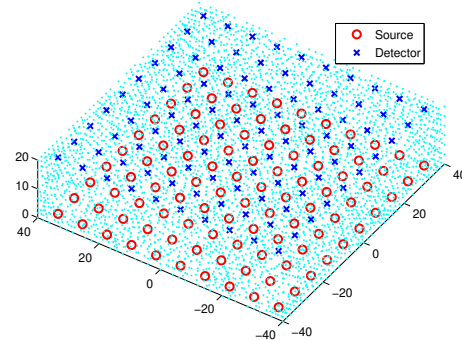
$20 \times 20 \times 10$ pixels was used.[1]

The input data for the reconstruction were obtained from a forward simulation. The sources were modeled as isotropic point sources radiating with 1 W situated at a distance of one scattering event inside the phantom.[2] The collected fluorescence was taken as the calculated boundary data. Figure 4.5 shows the typical fluorescence detected at the boundary for a fluorophore.

Reconstructed Results

The reconstructions of the traditional linear fluorophore and the upconverting quadratic fluorophore for two different source separations and detector separations are presented in Fig. 4.6. The source and detector grids were uniformly spaced in a square. Due to computational limitations, the number of source-

---

[1]There are several strategies for choosing reconstruction bases. Two examples are the second-mesh basis and the pixel basis [79, 80]. All strategies, however, aim to reduce the number of unknowns in the problem. This is motivated since the solution is expected to be smooth and using a coarser basis improves the ill-posedness. In this thesis the pixel basis was chosen, which is a set of regularly spaced pixels. This basis is suitable for problems with no spatial *a priori* information [81].

[2]The source power can of course be scaled based on a real experimental power. However, in the case of a normalized-Born approach, it should not influence on the calculated sensitivity profiles.
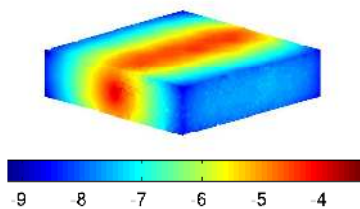
Fig. 4.5: Figure of the boundary fluorescence data obtained from forward simulations. The rod is clearly visible on the side of the slab. The colorbar shows the fluence rate $(\mathrm{W/mm^2})$ in $\log_{10}$ scale.

detector pairs was limited and kept to 10^4. As the sources and detectors were placed more tightly, this resulted in a smaller reconstruction region as seen in Fig. 4.6 (d–e).

As presented in Fig. 4.6, if one does not compensate for the quadratic power dependence of the nanoparticles, the reconstruction does not work at all.
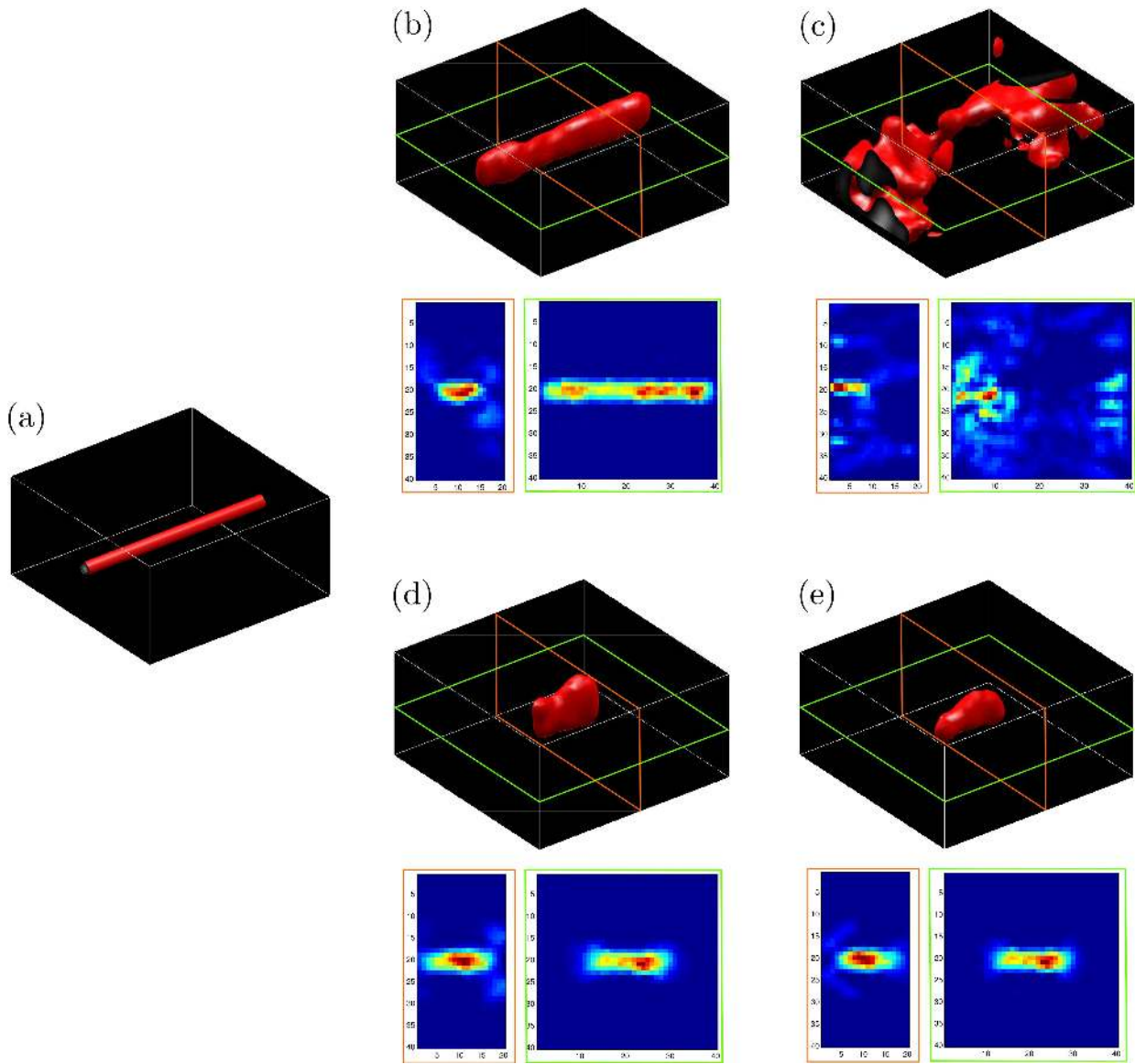
Fig. 4.6: Figures of the reconstructed results for two different spacings of the sources and detectors. The colored boxes represent the positions of the cross sections shown below each 3-D reconstruction image. (a) The ground truth target. (b) Reconstructed data using a linear fluorophore for detector spacing and source spacing of 8 mm. (c) Reconstructed data using a quadratic fluorophore for detector spacing and source spacing of 8 mm. (d) Reconstructed data using a linear fluorophore for detector spacing and source spacing of 3 mm. (e) Reconstructed data using a quadratic fluorophore for detector spacing and source spacing of 3 mm.

Concluding Remarks and Outlook

This thesis presents a study of upconverting luminescence imaging and tomography. It was shown that imaging with the upconverting nanocrystals is possible in scattering media resembling biological tissue. Furthermore, simulations showed that it is possible to adapt the theory used in fluorescent optical tomography, to work with the upconverting nanocrystals.

The particles used in this thesis, in comparison with organic fluorophores, were not very bright. Despite this, it is to our belief that they have a good chance to become an important biological marker in the future due to their unique optical properties. Detecting the very weak signal from the particles can be a challenge in an imaging setup. However, this is merely a technical issue that can be overcome by increasing the signal-to-noise ratio by using a more sensitive detector or a more powerful light source. When using Stokes-shifted fluorophores, increasing the signal-to-noise ratio will in general not boost the signal quality, since these fluorophores are ultimately limited by the signal-to-background contrast due to the ubiquitous tissue autofluorescence.

In this thesis, the particles were excited with CW light. Using a pulsed light source with high peak power should further increase the signal tremendously, due to the quadratic pump-power dependence of the upconverting process. Such a light source would still be harmless in terms of tissue heating and damaging, since the mean power can be kept low. When using a pulsed light source, good care should be taken to ensure that the pulse lengths are sufficient for the rise and decay times of the upconverting processes.

In the field of two-photon microscopy, fluorophores are excited through two-photon absorption which in turn emits light at double frequency. This process is very inefficient. It is possible that upconverting nanocrystals would be a more suitable fluorophore also in the field of microscopy.

The long-term effects of nanoparticles are often omitted in discussions. We believe that it is of the utmost importance to note that the long-term effects of water-soluble and/or functionalized nanoparticles are not yet fully understood. Even though coatings can be very stable chemically, investigations of the long

term effects are still needed.

Overall, at the current rate of which the upconverting nanoparticles are developing, they may very well be envisaged as important biological markers for tissue imaging purposes.

Bibliography

[1] D. H. Griffel. *Applied Functional Analysis*. Dover Publications, inc., New York, second edition, 2002.

[2] R. R. Anderson and J. A. Parrish. The Optics of Human Skin. *Journal of Investigative Dermatology*, **77**, 1:13–19, 1981.

[3] A. J. Welsh and M. J. van Gemert, editors. *Optical-Thermal Response of Laser-Irradiated Tissue*. Plenum Press, 1995.

[4] J. M. Schmitt and G. Kumar. Optical scattering properties of soft tissue: a discrete particle model. *Applied Optics*, **37**, 13:2788–2797, 1998.

[5] G. Alexandrakis, F. R. Rannou and A. F. Chatziioannou. Tomographic bioluminescence imaging by use of a combined optical-PET (OPET) system: a computer simulation feasibility study. *Physics in Medicine and Biology*, **50**, 17:4225–4241, 2005.

[6] V. Tuchin. *Tissue Optics*. SPIE Press, second edition, 2007.

[7] T. Svensson. *Pharmaceutical and Biomedical Applications of Spectroscopy in the Photon Migration Regime*. Ph.D. thesis, Lund University Lund Reports on Atomic Physics, LRAP 392, 2008.

[8] G. Mie. Beiträge zur Optik trüber Median, speziell kolloidaler Metallösungen. *Ann. Phys.*, **330**:377–445, 1908.

[9] W. M. S. Georges A. Wagnieres and B. C. Wilson. In Vivo Fluorescence Spectroscopy and Imaging for Oncological Applications. *Photochemistry and Photobiology*, **68(5)**:603–632, 1998.

[10] S. Andersson-Engels and B. Wilson. In vivo fluorescence in clinical oncology: fundamental and pratical issues. *Journal of Cell Pharmacol*, **3**:48–61, 1992.

[11] P. Diagaradjane, M. A. Yaseen, J. Yu, M. S. Wong and B. Anvari. Autofluorescence characterization for the early diagnosis of neoplastic changes in DMBA/TPA-induced mouse skin carcinogenesis. *Lasers in Surgery and Medicine*, **37**, 5:382–395, 2005.

[12] D. Farkas, C. Du, G. Fisher, C. Lau, W. Niu, E. Wachman and R. Levenson. Non-invasive image acquisition and advanced processing in optical bioimaging. *Computerized Medical Imaging and Graphics*, **22**, 2:89–102, 1998.

[13] B. Ballou, B. Lagerholm, L. Ernst, M. Bruchez and A. Waggoner. Noninvasive imaging of quantum dots in mice. *Bioconjugate Chemistry*, **15**:79–86, 2004.

[14] X. Gao, Y. Cui, R. M. Levenson, L. W. K. Chung and S. Nie. In vivo cancer targeting and imaging with semiconductor quantum dots. *Nature Biotechnology*, **22**, 8:969–976, 2004.

[15] M. Bruchez, M. Moronne, P. Gin, S. Weiss and A. Alivisatos. Semiconductor nanocrystals as fluorescent biological labels. *Science*, **281**:2013–2016, 1998.

[16] V. Karabanovas, E. Zakarevicius, A. Sukackaite, G. Streckyte and R. Rotomskis. Examination of the stability of hydrophobic (CdSe)ZnS quantum dots in the digestive tract of rats. *Photochemical & Photobiological Sciences*, **7**, 6:725–729, 2008.

[17] A. O. Choi, S. E. Brown, M. Szyf and D. Maysinger. Quantum dot-induced epigenetic and genotoxic changes in human breast cancer cells. *Journal of Molecular Medicine*, **86**, 3:291–302, 2008.

[18] S. Heer, K. Kompe, H. Güdel and M. Haase. Highly efficient multicolour upconversion emission in transparent colloids of lanthanide-doped $NaYF_4$ nanocrystals. *Advanced Materials*, **16**:2102–2105, 2004.

[19] J. Shan and Y. Ju. Controlled synthesis of lanthanide-doped $NaYF_4$ upconversion nanocrystals via ligand induced crystal phase transition and silica coating. *Applied Physics Letters*, **91**, 12, 2007.

[20] J. Swartling. *Biomedical and Atmospheric Applications of Optical Spectroscopy in Scattering Media*. Ph.D. thesis, Lund University Lund Reports on Atomic Physics, LRAP 290, 2002.

[21] J. C. Schotland. Continuous-wave diffusion imaging. *Journal of the Optical Society of America A-Optics Image Science and Vision*, **14**, 1:275–279, 1997.

[22] J. R. Mourant, J. P. Freyer, A. H. Hielscher, A. A. Eick, D. Shen and T. M. Johnson. Mechanisms of light scattering from biological cells relevant to noninvasive optical-tissue diagnostics. *Applied Optics*, **37**, 16:3586–3593, 1998.

[23] L. G. Henyey and J. L. Greenstein. Diffuse radiation in the galaxy. *Astrophysical Journal*, **93**, 1:70–83, 1941.

[24] P. Y. Liu. A New Phase Function Approximating To Mie Scattering For Radiative Transport Equations. *Physics in Medicine and Biology*, **39**, 6:1025–1036, 1994.

[25] L. Reynolds, C. Johnson and A. Ishimaru. Diffuse Reflectance From A Finite Blood Medium - Applications To Modeling Of Fiber Optic Catheters. *Applied Optics*, **15**, 9:2059–2067, 1976.

[26] S. R. Arridge and M. Schweiger. Image reconstruction in optical tomography. *Philosophical Transactions of the Royal Society B-Biological Sciences*, **352**, 1354:717–726, 1997.

[27] G. Marchesini, B. R. Webber, G. Abbiendi, I. G. Knowles, M. H. Seymour and L. Stanco. Herwig 5.1 - A Monte-Carlo Event Generator For Simulating Hadron Emission Reactions With Interfering Gluons. *Computer Physics Communications*, **67**, 3:465–508, 1992.

[28] A. Z. Panagiotopoulos. Direct Determination Of Phase Coexistence Properties Of Fluids By Monte-Carlo Simulation In A New Ensemble. *Molecular Physics*, **61**, 4:813–826, 1987.

[29] H. Bassler. Charge Transport In Disordered Organic Photoconductors - A Monte-Carlo Simulation Study. *Physica Status Solidi B-Basic Research*, **175**, 1:15–56, 1993.

[30] B. C. Wilson and G. Adam. A Monte-Carlo Model For The Absorption And Flux Distributions Of Light In Tissue. *Medical Physics*, **10**, 6:824–830, 1983.

[31] T. Kasemets. *Relic Gravitational Waves as a Source of CMB Polarization.* Bachelor thesis, Lund University, 2008.

[32] L. H. Wang, S. L. Jacques and L. Q. Zheng. Mcml - Monte-Carlo Modeling Of Light Transport In Multilayered Tissues. *Computer Methods and Programs in Biomedicine*, **47**, 2:131–146, 1995.

[33] E. Alerstam, T. Svensson and S. Andersson-Engels. Parallel computing with graphics processing units for high speed Monte Carlo simulation of photon migration. *Journal of Biomedical Optics Letters*, **accepted**, 2008.

[34] J. Coster and H. B. Hart. A Simple Proof of the Addition Theorem for Spherical Harmonics. *American Journal of Physics*, **59**, 4:371–373, 1991.

[35] S. R. Arridge. Topical Review: Optical tomography in medical imaging. *Inverse Problems*, **15**, 2:R41–R93, 1999.

[36] K. Furutsu and Y. Yamada. Diffusion-Approximation For A Dissipative Random Medium And The Applications. *Physical Review E*, **50**, 5:3634–3640, 1994.

[37] T. Durduran, A. G. Yodh, B. Chance and D. A. Boas. Does the photon-diffusion coefficient depend on absorption? *Journal of the Optical Society of America A-Optics Image Science and Vision*, **14**, 12:3358–3365, 1997.

[38] D. A. Boas. *Diffuse Photon Probes of Structural and Dynamical Properties of Turbid Media: Theory and Biomedical Applications.* Ph.D. thesis, University of Pennsylvania, 1996.

[39] G. Alexandrakis, T. J. Farrell and M. S. Patterson. Accuracy of the diffusion approximation in determining the optical properties of a two-layer turbid medium. *Applied Optics*, **37**, 31:7401–7409, 1998.

[40] B. E. A. Saleh and M. C. Teich. *Fundamentals of Photonics*. Wiley Series in Pure and Applied Optics. John Wiley & Sons, second edition, 2007.

[41] N. Bloembergen. Solid State Infraread Quantum Counters. *Physical Review Letters*, **2**, 3:84–85, 1959.

[42] F. Auzel. Upconversion and anti-stokes processes with f and d ions in solids. *Chemical Reviews*, **104**, 1:139–173, 2004.

[43] S. Svanberg. *Atomic and Molecular Spectroscopy: Basic Aspects and Practical Applications*. Springer, fourth edition, 2004.

[44] C. J. Foot. *Atomic Physics*. Oxford Master Series in Atomic, Optical and Laser Physics. Oxford University Press, 2005.

[45] M. Pollnau, D. Gamelin, S. Luthi, H. Gudel and M. Hehlen. Power dependence of upconversion luminescence in lanthanide and transition-metal-ion systems. *Physical Review B*, **61**, 5:3337–3346, 2000.

[46] F. Vetrone and J. A. Capobianco. Lanthanide-doped fluoride nanoparticles: luminescence, upconversion, and biological applications. *International Journal of Nanotechnology*, **5**, 9-12:1306–1339, 2008.

[47] J. Suyver, J. Grimm, M. van Veen, D. Biner, K. Kramer and H. Gudel. Upconversion spectroscopy and properties of NaYF$_4$ doped with Er^{3+}, Tm^{3+} and/or Yb^{3+}. *Journal of Luminescence*, **117**, 1:1–12, 2006.

[48] K. Kramer, D. Biner, G. Frei, H. Gudel, M. Hehlen and S. Luthi. Hexagonal sodium yttrium fluoride based green and blue emitting upconversion phosphors. *Chemistry of Materials*, **16**, 7:1244–1251, 2004.

[49] A. Aebischer, S. Heer, D. Biner, K. Kramer, M. Haase and H. Gudel. Visible light emission upon near-infrared excitation in a transparent solution of nanocrystalline beta-NaGdF4 : Yb3+, Er3+. *Chemical Physics Letters*, **407**, 1-3:124–128, 2005.

[50] J. Boyer, F. Vetrone, L. Cuccia and J. Capobianco. Synthesis of colloidal upconverting NaYF4 nanocrystals doped with Er3+, Yb3+ and Tm3+, Yb3+ via thermal decomposition of lanthanide trifluoroacetate precursors. *Journal of the American Chemical Society*, **128**, 23:7444–7445, 2006.

[51] P. Diamente and F. Veggel. Water-Soluble Ln^{3+}-Doped LaF$_3$ Nanoparticles: Retention of Strong Luminescence and Potential as Biolabels. *Journal of Fluorescence*, **15**, 4:543–551, 2005.

[52] M. N. V. R. Kumar. A review of chitin and chitosan applications. *Reactive & Functional Polymers*, **46**, 1:1–27, 2000.

[53] F. Wang, Y. Zhang, X. P. Fan and M. Q. Wang. One-pot synthesis of chitosan/LaF$_3$:Eu^{3+} nanocrystals for bio-applications. *Nanotechnology*, **17**, 5:1527–1532, 2006.

[54] G. S. Yi and G. M. Chow. Water-soluble NaYF$_4$:Yb,Er(Tm)/NaYF$_4$/-polymer core/shell/shell nanoparticles with significant enhancement of upconversion fluorescence. *Chemistry Of Materials*, **19**, 3:341–343, 2007.

[55] M. Darbandi and T. Nann. One-pot synthesis of YF_3@silica core/shell nanoparticles. *Chemical Communications*, , 7:776–778, 2006.

[56] H. Ow, D. R. Larson, M. Srivastava, B. A. Baird, W. W. Webb and U. Wiesner. Bright and stable core-shell fluorescent silica nanoparticles. *Nano Letters*, **5**, 1:113–117, 2005.

[57] F. Wang, Y. Zhang, X. P. Fan and M. Q. Wang. Facile synthesis of water-soluble $LaF_3:Ln^{3+}$ nanocrystals. *Journal of Materials Chemistry*, **16**, 11:1031–1034, 2006.

[58] H. C. Lu, G. S. Yi, S. Y. Zhao, D. P. Chen, L. H. Guo and J. Cheng. Synthesis and characterization of multi-functional nanoparticles possessing magnetic, up-conversion fluorescence and bio-affinity properties. *Journal of Materials Chemistry*, **14**, 8:1336–1341, 2004.

[59] L. Y. Wang and Y. D. Li. Green upconversion nanocrystals for DNA detection. *Chemical Communications*, , 24:2557–2559, 2006.

[60] G. Yi, H. Lu, S. Zhao, G. Yue, W. Yang, D. Chen and L. Guo. Synthesis, characterization, and biological application of size-controlled nanocrystalline $NaYF_4:Yb,Er$ infrared-to-visible up-conversion phosphors. *Nano Letters*, **4**, 11:2191–2196, 2004.

[61] Q. Lue, A. Li, F. Guo, L. Sun and L. Zhao. Experimental study on the surface modification of $Y_2O_3:Tm^{3+}/Yb^{3+}$ nanoparticles to enhance upconversion fluorescence and weaken aggregation. *Nanotechnology*, **19**, 14, 2008.

[62] W. C. Martin, R. Zalubas and L. Hagan. *Atomic Energy Levels: The Rare-Earth Elements*. U.S. Department of Commerce, National Bureau of Standards, 1978.

[63] V. Ntziachristos. Fluorescence molecular imaging. *Annual Review of Biomedical Engineering*, **8**:1–33, 2006.

[64] S. R. Arridge and M. Schweiger. Image reconstruction in optical tomography, 1997. Philosophical Transactions of the Royal Society B-Biological Sciences.

[65] S. C. Davis, H. Dehghani, J. Wang, S. Jiang, B. W. Pogue and K. D. Paulsen. Image-guided diffuse optical fluorescence tomography implemented with Laplacian-type regularization. *Optics Express*, **15**, 7:4066–4082, 2007.

[66] M. OLeary, D. Boas, X. Li, B. Chance and A. Yodh. Fluorescence lifetime imaging in turbid media. *Optics Letters*, **21**, 2:158–160, 1996.

[67] A. Ishimaru. Theory And Application Of Wave-Propagation And Scattering In Random Media. *Proceedings of the IEEE*, **65**, 7:1030–1061, 1977.

[68] R. A. J. Groenhuis, H. A. Ferwerda and J. J. Tenbosch. Scattering And Absorption Of Turbid Materials Determined From Reflection Measurements. *Applied Optics*, **22**, 16:2456–2462, 1983.

[69] M. Schweiger, S. R. Arridge, M. Hiraoka and D. T. Delpy. The Finite-Element Method For The Propagation Of Light In Scattering Media - Boundary And Source Conditions. *Medical Physics*, **22**, 11:1779–1792, 1995.

[70] G. Y. Panasyuk, Z. M. Wang, J. C. Schotland and V. A. Markel. Fluorescent optical tomography with large data sets. *Optics Letters*, **33**, 15:1744–1746, 2008.

[71] V. A. Markel and J. C. Schotland. Symmetries, inversion formulas, and image reconstruction for optical tomography. *Physical Review E*, **70**, 5:056616, 2004.

[72] E. Süli and D. F. Mayers. *An Introduction to Numerical Analysis*. Cambridge University Press, 2003.

[73] G. Strang and G. J. Fix. *An Analysis of the Finite Element Method*. Prentice-Hall, 1973.

[74] H. Dehghani, B. W. Pogue, S. D. Jiang, B. Brooksby and K. D. Paulsen. Three-dimensional optical tomography: resolution in small-object imaging. *Applied Optics*, **42**, 16:3117–3128, 2003.

[75] R. Penrose. A generalized inverse for matrices. *Proc. Cambridge Philos. Soc.*, **51**:406–413, 1955.

[76] C. T. Xu, N. Svensson, J. Axelsson, P. Svenmarker, G. Somesfalean, G. Chen, H. Liang, H. Liu, Z. Zhang and S. Andersson-Engels. Autofluorescence insensitive imaging using upconverting nanocrystals in scattering media. *Applied Physics Letters*, **93**, 17:171103, 2008.

[77] E. Alerstam, S. Andersson-Engels and T. Svensson. White Monte Carlo for time-resolved photon migration. *Journal of Biomedical Optics*, **13**, 4:041304, 2008.

[78] V. Ntziachristos, E. Schellenberger, J. Ripoll, D. Yessayan, E. Graves, A. Bogdanov, L. Josephson and R. Weissleder. Visualization of antitumor treatment by means of fluorescence molecular tomography with an annexin V-Cy5.5 conjugate. *Proceedings of the National Academy of Sciences of the United States of America*, **101**:12294–12299, 2004.

[79] K. D. Paulsen, P. M. Meaney, M. J. Moskowitz and J. M. Sullivan. A Dual Mesh Scheme For Finite-Element Based Reconstruction Algorithms. *IEEE Transactions on Medical Imaging*, **14**, 3:504–514, 1995.

[80] M. Schweiger and S. R. Arridge. Optical tomographic reconstruction in a complex head model using a priori region boundary information. *Physics in Medicine and Biology*, **44**, 11:2703–2721, 1999.

[81] S. C. Davis, H. Dehghani, J. Wang, S. Jiang, B. W. Pogue and K. D. Paulsen. Image-guided diffuse optical fluorescence tomography implemented with Laplacian-type regularization. *Optics Express*, **15**, 7:4066–4082, 2007.

Index

Paper

Autofluorescence insensitive imaging using upconverting nanocrystals in scattering media

Can T. Xu, Niclas Svensson, Johan Axelsson, Pontus Svenmarker, Gabriel Somesfalean, Guanying Chen, Huijuan Liang, Haichun Liu, Zhiguo Zhang, and Stefan Andersson-Engels

We designed and performed the experiments and wrote the manuscript.

Autofluorescence insensitive imaging using upconverting nanocrystals in scattering media

Can T. Xu,[1,a] Niclas Svensson,[1] Johan Axelsson,[1] Pontus Svenmarker,[1]
Gabriel Somesfalean,[1] Guanying Chen,[2] Huijuan Liang,[2] Haichun Liu,[2] Zhiguo Zhang,[2]
and Stefan Andersson-Engels[1]

[1]*Department of Physics, Lund University, P.O. Box 118, S-221 00 Lund, Sweden*
[2]*Department of Physics, Harbin Institute of Technology, P.O. Box 3025, Harbin 150080,
People's Republic of China*

Autofluorescence is a nuisance in the field of fluorescence imaging and tomography of exogenous molecular markers in tissue, degrading the quality of the collected data. In this letter, we report autofluorescence insensitive imaging using highly efficient upconverting nanocrystals ($NaYF_4$:Yb^{3+}/Tm^{3+}) in a tissue phantom illuminated with near-infrared radiation of 85 mW/cm^2. It was found that imaging with such nanocrystals leads to an exceptionally high contrast compared to traditional downconverting fluorophores due to the absence of autofluorescence. Upconverting nanocrystals may be envisaged as important biological markers for tissue imaging purposes. © 2008 American Institute of Physics. [DOI: 10.1063/1.3005588]

In recent years, the interest for fluorescence diffuse optical imaging and tomography has grown tremendously.[1–3] Much of the work has been focused on developing inexpensive and compact systems for macroscopic imaging of fluorophores embedded in small animals. The systems could, for example, be used to monitor the effects from drugs on cancer tumors over a period of time, without sacrificing the animals. Extensive research has been performed both on the practical and the theoretical side in this area. Currently, mainly traditional dyes are used as fluorophores. These dyes emit Stoke shifted light upon excitation, and can be very effective with quantum efficiencies close to unity. However, since tissue itself autofluoresces due to several endogenous fluorophores mainly in the skin, a background fluorescence from the bulk tissue will always exist.[4,5] In the presence of tissue autofluorescence, different spectral unmixing algorithms can also be used to extract the signal. These algorithms utilize the spectral characteristics of the fluorophores and the autofluorescence.[6] However, the measurement procedure can be quite complex since one needs to acquire the emission at multiple wavelengths. To suppress the effects of autofluorescence, several approaches have been suggested. The two most promising ones are based on quantum dots and upconverting markers.

Quantum dots have been used as fluorophores in a great number of studies.[7–9] Their large Stoke shift and narrow emission spectra allow the emission to be detected in a spectral band with low tissue autofluorescence. Quantum dots are very bright fluorophores due to their high absorption, mainly in the UV region. Their emission wavelength is dependent on the core size and can be selected over a wide range while the same excitation wavelength can be used.[7] The main drawback at this stage for these fluorophores is their toxicity, together with the fact that penetration of the UV light is low in tissue. Typical quantum dots are based on CdSe due to the well established fabrication technology.[10] Recent studies have shown that these quantum dots are potentially harmful

to organisms.[11,10] The quantum dots tend to destabilize when exposed to biological environments. Adding the fact that they can easily penetrate into cells, the damage can be quite substantial. Research, however, is underway to produce less harmful quantum dots, as well as enhancing their biocompatibility.[12]

Upconverting nanoparticles have been proposed as a fluorophore in biomedical imaging applications due to their unique property to efficiently emit anti-Stoke shifted light upon near-infrared excitation.[13,14] The main challenge has been to develop upconverting markers with high-quantum yield in the wavelength region above 650 nm where tissue is relatively transparent.

In this letter, we demonstrate autofluorescence insensitive imaging with novel high-quantum yield upconverting nanoparticles emitting at 800 nm. The study is performed in a controlled environment within tissue phantoms in which autofluorescence is simulated, and comparison with ordinary Stoke shifted fluorophores emitting at the same wavelength is made.

Efficient upconverting phosphors of nanometer size have been fabricated.[14] The particles are doped with Yb^{3+}, which acts as sensitizer, and another rare earth ion, which acts as activator.[15] By using different activators, various emission wavelengths can be accomplished with the same excitation wavelength. It has been shown that $NaYF_4$ is the most efficient host known for upconverting phosphorous crystals.[16] In this study, highly efficient $NaYF_4$ crystals doped with Yb^{3+} and Tm^{3+} were used, which were prepared according to the procedure described in detail in Ref. 17. The particles absorb light at 980 nm and emit upconverted light at 800 nm. The process involves absorption of two or more photons with an intermediate metastable state.[15] Figure 1 shows the emission spectrum for the nanoparticles, the blue emission line at 477 nm is only visible for higher pump intensities. The pump-power dependence of the 800 nm line was measured to be quadratic (slope=2.0) using low intensities, as seen in the inset of Fig. 1, suggesting a two-photon process.
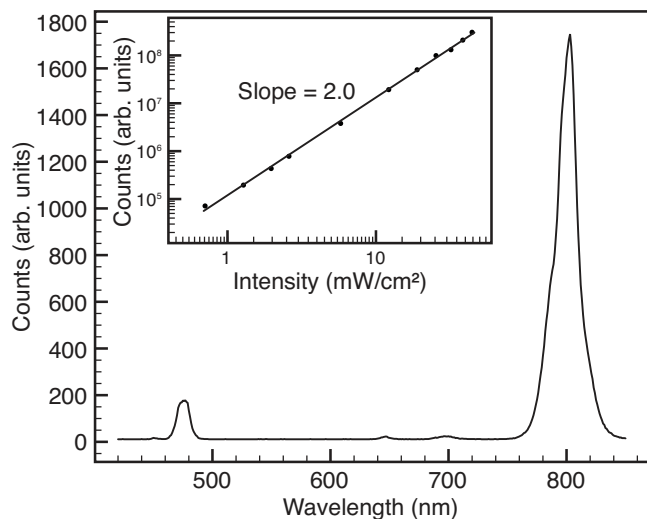
[a]Electronic mail: can.xu@fysik.lth.se.

FIG. 1. Emission spectrum recorded for the nanoparticles under 980 nm excitation with an intensity of 6 W/cm^2. The inset shows the pump-power dependence of the interesting 800 nm line measured under low intensities.

FIG. 3. Images comparing the DY-781 dye and the nanoparticles with and without autofluorescence, along with plots showing the sums in the vertical directions. The white dots have been added artificially and represent the positions used for the excitation light. The left column shows the results using DY-781, and the right column shows the results using upconverting nanoparticles. (a) and (b) are taken without any added autofluorophores. (c) and (d) are taken with a background autofluorophore concentration of 40 nM.

A tissue phantom consisting of water, intralipid, and ink was prepared. The optical properties of the tissue phantom were measured with a time-of-flight spectroscopy system,[18] and determined to have a reduced scattering coefficient μ_s' =6.5 cm^{-1} and an absorption coefficient μ_a=0.44 cm^{-1} for λ=660 nm. The parameters were chosen to have a good correspondence to real tissue in small animals.[19] Two capillary tubes with inner diameters of 2.4 mm were used as containers for the fluorophores.

The imaging system is schematically shown in Fig. 2. The tubes were submerged into the tissue phantom to a depth of 5.0 mm, where the depth was taken as the distance from the front surface of the tubes to the surface of the phantom. Fiber-coupled lasers were used to illuminate the phantom with a slightly divergent beam. The spot sizes of the lasers on the phantom were approximately 1 cm^2. An air cooled charge coupled device (CCD) camera captured the images through a set of dielectric bandpass filters centered at 800 nm.

The first tube was filled with a solution of the nanocrystals dissolved in dimethyl sulfoxide (DMSO) with a concentration of 1 wt %. To excite the nanoparticles, a 978 nm laser diode was used, with a power of approximately 85 mW on
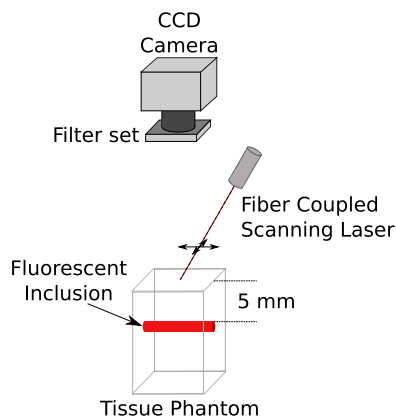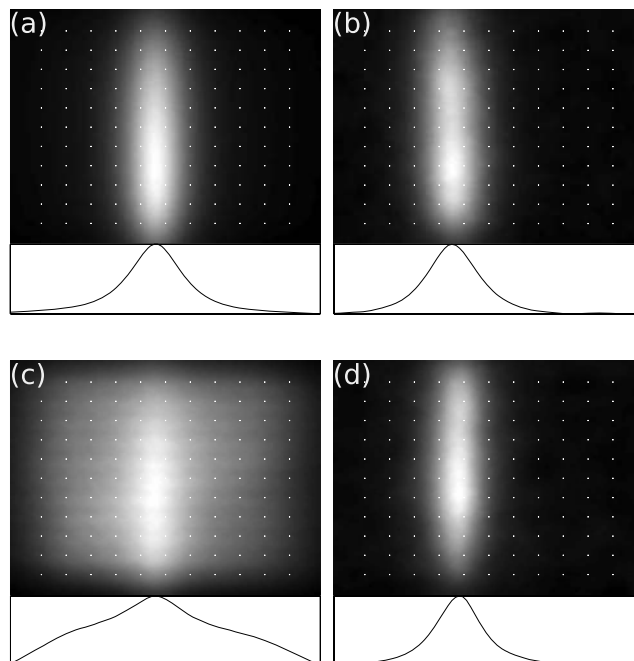

FIG. 2. (Color online) Schematic of the imaging setup. Light from a fiber-coupled laser is scanned in an array on the surface of the phantom. An air cooled CCD camera is used to capture an image for every scanned position.

the surface of the tissue phantom. The second tube was filled with a solution of ordinary fluorophores (DY-781, Dyomics GmbH) dissolved in ethanol with a concentration of 1 μM. The fluorophores were excited with a 780 nm laser diode with a power of 40 mW on the surface of the phantom. The concentration of the nanoparticles is reasonably consistent with studies performed using quantum dots *in vivo*. In those studies, approximately 1 nmol of CdSe quantum dots were injected into a mouse ($\sim$18 g), giving an approximate concentration of 0.01 wt % if distributed homogeneously.[8,9] With functionalized quantum dots, selective accumulation in tumors can be achieved. Taking this into consideration and the fact that the nanoparticles have molar mass of the same order of magnitude as the quantum dots, the concentration of 1 wt % used in this study seems acceptable.

The lasers were raster scanned in a 4.4$\times$4.4 cm^2 array consisting of 121 positions, and an image was acquired for every laser position. In order to minimize the effects of random bright pixels, a median filter with a mask of 3 $\times$3 pixels was applied to all images. The individual images were then summed, and a representation of the photon distribution on the surface was obtained. Even if this does not accurately reflect the fluorophore distribution, it enables detection of fluorescent inclusions. To mimic tissue autofluorescence, a small amount of DY-781 was also added into the phantom.

Figure 3 shows images taken with and without autofluorescence. As expected, the autofluorescence effectively hides the signal from the inclusion with the ordinary fluorophores [Fig. 3(c)], while no background appears on the images using the upconversion scheme [Fig. 3(d)]. It is worth to notice that using traditional fluorophores, even without any artificial

autofluorophores added, the autofluorescence introduced by the intralipid within the phantom is visible, see the cross section profile in Fig. 3(a).

As seen in Fig. 3, the signal-to-background contrast is superior for upconverting nanoparticles emitting in a wavelength region where no Stoke shifted tissue autofluorescence is present. Higher excitation power can increase the signal-to-noise ratio, without sacrificing the high contrast. Increasing the signal-to-noise ratio, however, will not boost the image quality using traditional fluorophores since they are limited by a lower signal-to-background contrast due to the ubiquitous autofluorescence. Even with the lower quantum efficiency of the nanoparticles compared to traditional fluorophores the image quality is therefore expected to be better.

Background caused by autofluorescence is very prominent when working with an epifluorescence imaging setup in comparison to a fluorescence transmission imaging setup. In the latter setup, it is possible to suppress the autofluorescence signal fairly effectively.[20] However, such a system can be very ineffective when used to detect and image a superficial signal.

The particles used for this study were still in the development stage. For example, they were in bulk state without any kind of coating, and thus not soluble in water and therefore not biocompatible. However, improved fabrication methods can make them water soluble.[21,22] In addition, there are also reports suggesting that coating the particles with an undoped layer reduces the nonradiative losses at the surface, thus effectively enhancing their upconversion efficiency.[22,23] Using a pulsed light source with a higher peak power should further increase the signal tremendously, due to the quadratic pump-power dependence of the upconverting process. Such a light source should still be harmless in terms of tissue heating and damaging, since the mean power can still be kept low.

Future work will involve the use of nanocrystals for diffuse optical tomography. With their unique features in emitting a signal that is insensitive to the downconverting autofluorescence, they have the potential to become an important biological marker. In a longer perspective we hope to functionalize the particles with tumor seeking properties. Early studies by other groups have already been performed, and the prospects are very promising.[24]

[1]V. Ntziachristos, Annu. Rev. Biomed. Eng. **8**, 1 (2006).

[2]V. Ntziachristos, J. Ripoll, L. Wang, and R. Weissleder, Nat. Biotechnol. **23**, 313 (2005).

[3]L. Sampath, W. Wang, and E. M. Sevick-Muraca, J. Biomed. Opt. **13**, 041312 (2008).

[4]G. Wagnieres, W. Star, and B. Wilson, Photochem. Photobiol. **68**, 603 (1998).

[5]S. Andersson-Engels and B. Wilson, J. Cell Pharmacol **3**, 48 (1992).

[6]D. Farkas, C. Du, G. Fisher, C. Lau, W. Niu, E. Wachman, and R. Levenson, Comput. Med. Imaging Graph. **22**, 89 (1998).

[7]M. Bruchez, M. Moronne, P. Gin, S. Weiss, and A. Alivisatos, Science **281**, 2013 (1998).

[8]X. Gao, Y. Cui, R. M. Levenson, L. W. K. Chung, and S. Nie, Nat. Biotechnol. **22**, 969 (2004).

[9]B. Ballou, B. Lagerholm, L. Ernst, M. Bruchez, and A. Waggoner, Bioconjugate Chem. **15**, 79 (2004).

[10]V. Karabanovas, E. Zakarevicius, A. Sukackaite, G. Streckyte, and R. Rotomskis, Photochem. Photobiol. Sci. **7**, 725 (2008).

[11]A. O. Choi, S. E. Brown, M. Szyf, and D. Maysinger, J. Mol. Med. **86**, 291 (2008).

[12]W. B. Cai, A. R. Hsu, Z. B. Li, and X. Y. Chen, Nanoscale Res. Lett. **2**, 265 (2007).

[13]J. Shan and Y. Ju, Appl. Phys. Lett. **91**, 123103 (2007).

[14]S. Heer, K. Kompe, H. Güdel, and M. Haase, Adv. Mater. (Weinheim, Ger.) **16**, 2102 (2004).

[15]F. Auzel, Chem. Rev. (Washington, D.C.) **104**, 139 (2004).

[16]K. Kramer, D. Biner, G. Frei, H. Güdel, M. Hehlen, and S. Luthi, Nano Lett. **16**, 1244 (2004).

[17]G. Yi, H. Lu, S. Zhao, Y. Ge, W. Yang, D. Chen, and L.-H. Guo, Nano Lett. **4**, 2191 (2004).

[18]E. Alerstam, S. Andersson-Engels, and T. Svensson, J. Biomed. Opt. **13**, 041304 (2008).

[19]V. Ntziachristos, E. Schellenberger, J. Ripoll, D. Yessayan, E. Graves, A. Bogdanov, L. Josephson, and R. Weissleder, Proc. Natl. Acad. Sci. U.S.A. **101**, 12294 (2004).

[20]G. Zacharakis, H. Shih, J. Ripoll, R. Weissleder, and V. Ntziachristos, Mol. Imaging **5**, 153 (2006).

[21]F. Wang, D. K. Chatterjee, Z. Li, Y. Zhang, X. Fan, and M. Wang, Nanotechnology **17**, 5786 (2006).

[22]G.-S. Yi and G.-M. Chow, Chem. Mater. **19**, 341 (2007).

[23]J. Suyver, A. Aebischer, D. Biner, P. Gerner, J. Grimm, S. Heer, K. Kramer, C. Reinhard, and H. Güdel, Opt. Mater. (Amsterdam, Neth.) **27**, 1111 (2005).

[24]Q. Lü, F. Guo, L. Sun, A. Li, and L. Zhao, J. Phys. Chem. C **112**, 2836 (2008).